Illuminating pathways for nanoparticle superlattice self-assembly

Taylor J. Woehl

Check for updates

The final structure of nanoparticle self-assembly intimately depends on the assembly pathway, which has remained obscure due to a lack of sufficiently high-spatiotemporal-resolution direct imaging approaches. Now, combining liquid-cell transmission electron microscopy with molecular dynamics simulations uncovers the complete dynamics of solvent-dependent assembly and phase transitions of nanocube superlattices.

Macroscopic materials have functional properties determined by their composition and structure, such as the bandgap of semiconductors or thermal properties of refractory materials. On the other hand, nanoparticle superlattices, hierarchical crystalline materials where nanoparticles take the place of atoms, have optical, mechanical and electronic properties that strongly depend on the mesoscopic order of the nanoparticle building blocks[1,2]. Superlattices can be formed by subjecting nanoparticles dispersed in a liquid phase to environmental conditions that cause attractive interparticle interactions. However, nanoparticles have slower dynamics than atomic systems, which can lead to non-equilibrium structures[3]. Achieving the desired final structure is critical because the functional properties of self-assembled superlattices are rapidly degraded by defects[4]. Rational design requires intimate understanding of the self-assembly pathways and assembly dynamics. Methods for investigating the self-assembly pathway of nanoparticles have so far been limited to numerical simulations and ensemble-scale scattering experiments[5,6], which cannot probe nucleation, crystallization and defect-removal processes due to the wide timescale disparities of these physicochemical processes. Direct particle-scale imaging of the self-assembly pathway of colloidal nanoparticles would enable scientists to establish the underlying mechanisms by which kinetics and interparticle interactions impact assembly dynamics. If realized, these insights are expected to guide the rational design of fabrication conditions to self-assemble nanoparticle superlattices with minimal defects.

Now, writing in *Nature Chemical Engineering*, Glotzer, Ye and co-workers report the utilization of liquid-cell transmission electron microscopy (LC-TEM) and molecular dynamics simulations to uncover interparticle interaction-dependent non-classical crystallization pathways of gold nanocube superlattices[7]. The researchers used polymer-coated gold nanocubes as model anisotropic colloids and varied the polarity of the solvent to act on the interparticle interactions. LC-TEM was used to form nanoscale movies of the assembly dynamics starting from dispersed nanoparticles. Image analysis was deployed to measure various bond orientation parameters, which were used to unveil formation pathways of different crystalline superlattice phases.

With the aid of coarse-grained molecular dynamics simulations, the team identified electrostatic interactions between nanocubes, in particular, the electrostatic screening length, as a key parameter in determining the crystalline phase of the nanoparticle superlattice. Time-dependent bond-orientation parameters of the nanoparticle assemblies revealed complex, multistep crystallization processes. For instance, during the formation of the rhombic lattice, long-ranged translational order developed before orientational order, suggesting a non-classical crystallization mechanism. Indeed, the authors observed an intriguing phase transition from a metastable polycrystalline hexagonal phase to a polycrystalline rhombic lattice. Following this phase transition, orientational order mapping of superlattices revealed that a polycrystalline to single-crystal transition occurred via cooperative rotation of nanocubes at twin boundaries. These observations unveil the mechanism by which defects anneal from nanoparticle superlattices, which is a key process enabling formation of nearly perfect superlattices needed for optoelectronic applications. Conversely, an initially disordered liquid-like state preceded the formation of a hexagonal rotator phase when the electrostatic screening length was relatively large. Finally, a square-like lattice formed in the most polar solvent with the strongest attractive interparticle interactions. Here, small domains with a high local four-fold bond-orientation order parameter formed initially to maximize interparticle contact and progressively ripened into a large single square crystal. Beyond self-assembly of superlattices from dispersed nanoparticles, the authors directly observed reversible solid–solid phase transitions in nanoparticle superlattices. The team used rapid solvent exchange to modify interparticle interactions and observed rapid transformation between each of the phases discussed above. These phase transformations involved complex dynamics, including collective nanoparticle rotation and intermediate crystalline phases. Together, these observations reveal a previously unseen world of complex assembly pathways for nanoparticle superlattices and uncover the assembly mechanisms underlying process–structure relationships that can be tuned to rationally target desired structures.

A few open questions of the current work include the origin of the electrostatic interactions between the nanoparticles and the predicted electrostatic screening length. The authors suggest that nanocubes acquire charge via electron beam charging of the silicon nitride membrane and subsequent charge transfer to the nanoparticles[8]. Charged nanoparticles are expected to experience long-ranged (several micrometers) unscreened electrostatic interactions in non-aqueous solvents[9]. However, screening lengths on the order of 10 nm are predicted here, which is typically seen in aqueous systems. The alcohol solvents used here have relatively large Onsager lengths compared with water, which encourages ion recombination. One possibility is that rapid solvent radiolysis by the electron beam generates relatively high ion concentrations despite this propensity for ion recombination[10]. Despite these uncertainties, the LC-TEM observations of solvent-dependent interparticle

News & views

interactions are generally consistent with screened electrostatic interactions. Additional theoretical and experimental work will reveal the origins of the nanoparticle charging and electrostatic screening length.

The study of nanoparticle self-assembly dynamics using LC-TEM is expected to have a substantial impact on designing functional optical, electronic and mechanical materials from nanoparticles. One grand challenge in this field is to self-assemble nanoparticles into targeted macroscopic structures with minimal defects. Understanding how colloidal nanoparticles assemble into ordered structures, such as that observed in this work, represents a critical step toward developing strategies for rational design of nanoparticle superlattices.

Taylor J. Woehl ✉

Department of Chemical and Biomolecular Engineering, University of Maryland, College Park, College Park, MD, USA.
✉e-mail: tjwoehl@umd.edu

References

1. Santos, P. J., Gabrys, P. A., Zornberg, L. Z., Lee, M. S. & Macfarlane, R. J. *Nature* **591**, 586–591 (2021).
2. Si, K. J., Chen, Y., Shi, Q. & Cheng, W. *Adv. Sci.* **5**, 1700179 (2018).
3. Hueckel, T., Hocky, G. M., Palacci, J. & Sacanna, S. *Nature* **580**, 487–490 (2020).
4. Ondry, J. C., Philbin, J. P., Lostica, M., Rabani, E. & Alivisatos, A. P. *ACS Nano* **13**, 12322–12344 (2019).
5. Abécassis, B., Testard, F. & Spalla, O. *Phys. Rev. Lett.* **100**, 115504 (2008).
6. Missoni, L. L. & Tagliazucchi, M. *ACS Nano* **14**, 5649–5658 (2020).
7. Zhong, Y. et al. *Nat. Chem. Eng.* https://doi.org/10.1038/s44286-024-00102-9 (2024).
8. Woehl, T. J. & Prozorov, T. *J. Phys. Chem. C* **119**, 21261–21269 (2015).
9. Espinosa, C. E., Guo, Q., Singh, V. & Behrens, S. H. *Langmuir* **26**, 16941–16948 (2010).
10. Abellan, P. et al. *Langmuir* **32**, 1468–1477 (2016).

Competing interests

The author declares no competing interests.

Article

Engineering and direct imaging of nanocube self-assembly pathways

Yaxu Zhong[1,4], Timothy C. Moore [●][2,4], Tobias Dwyer [●][2,4], Alex Butrum-Griffith[1], Vincent R. Allen[1], Jun Chen [●][1], Yi Wang [●][1], Fanrui Cheng[1], Sharon C. Glotzer [●][2,3][✉] & Xingchen Ye [●][1][✉]

Nanoparticle self-assembly offers a scalable and versatile means to fabricate next-generation materials. The prevalence of metastable and nonequilibrium states during the assembly process makes the final structure and function directly dependent upon formation pathways. However, it remains challenging to steer the assembly pathway of a nanoparticle system toward multiple superstructures while visualizing in situ. Here we use liquid-cell transmission electron microscopy to image complete self-assembly processes of gold nanocubes, a model shape-anisotropic nanocolloidal system, into distinct superlattices. Theoretical analysis and molecular dynamics simulations indicate that the electrostatic screening of the medium dictates self-assembly pathways by its effects on the interactions between nanocubes. We leverage this understanding to demonstrate on-the-fly control of assembly behavior through rapid solvent exchange. Our joint experiment–simulation–theory investigation paves the way for elucidating the relationships among building block attributes, assembly pathways and superstructures in nanoscale assembly and opens new avenues for the bottom-up design of reconfigurable and adaptive metamaterials.

Fluid–solid and solid–solid transitions are central to the formation of natural and synthetic materials spanning many length scales. Examples include the crystallization of ice[1] and proteins[2], the formation of metal alloys[3], biomineralization[4], and self-assembly of nanoparticles[5] and micrometer-sized colloids[6] into ordered phases. With nanoscale building blocks, the ever-increasing structural diversity, complexity and reconfigurability of their self-organized superstructures promise to open new doors to developing next-generation functional materials and devices[7–21]. Understanding the mechanisms and pathways underlying ordering transitions is necessary to provide design guidelines for targeted structures and to refine existing models of phase transitions in atomic and colloidal systems. In comparison with predicting the final structures, forecasting ordering pathways from building block attributes such as shape anisotropy is far more difficult, even when the pairwise interactions are known. This difficulty arises from emergent
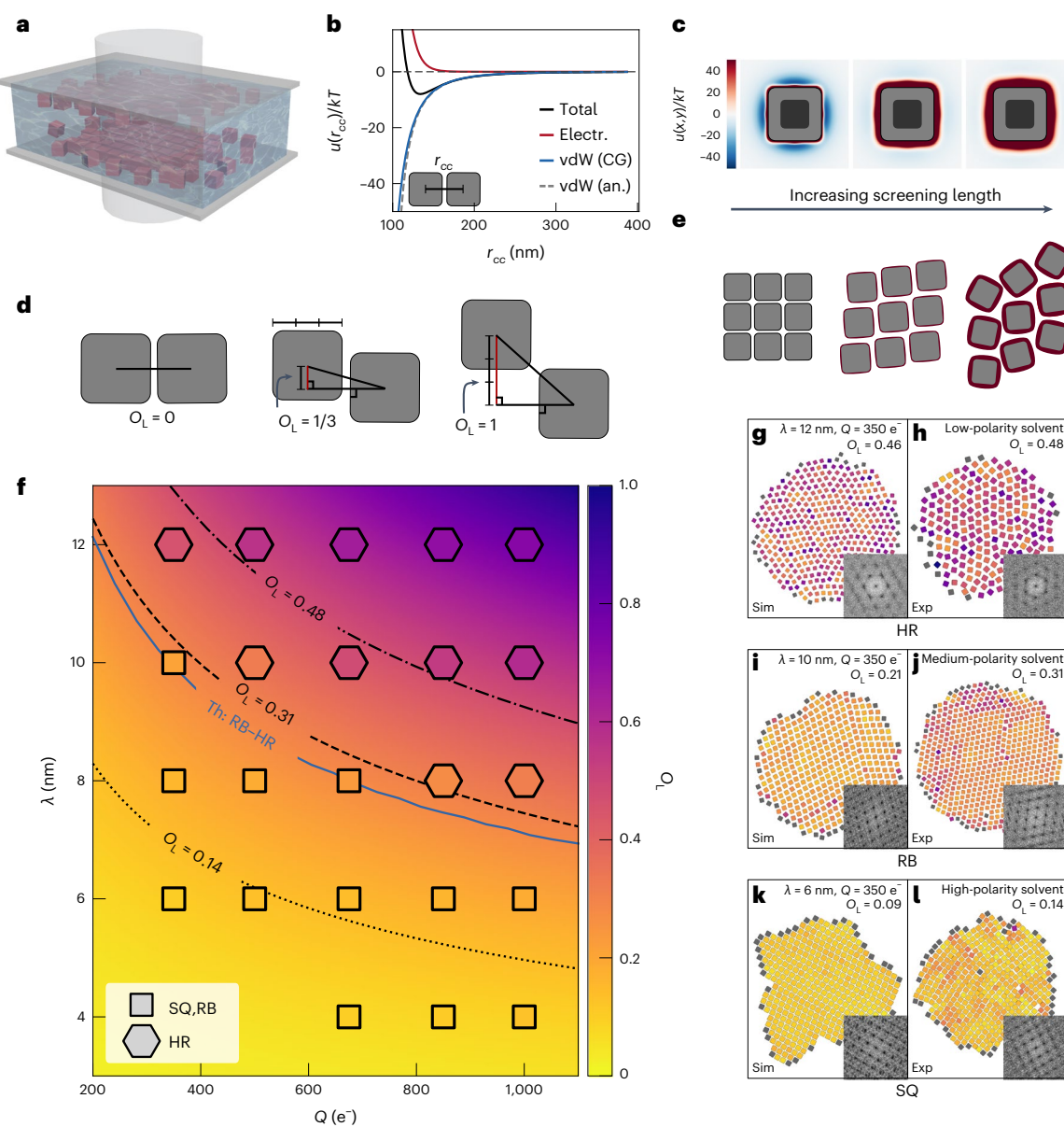
phenomena in ensembles of nanoparticles, for example, nonadditive interactions[22,23], prenucleation motifs[24,25] and multistep nucleation[26–30]. A critical first step in understanding building-block–pathway–superstructure relationships is direct observation of kinetic pathways from the appearance of the first crystalline nuclei to the equilibrium or steady-state superstructure. Optical microscopy has been widely used to directly visualize the dynamics of micrometer-scale colloids[31–35]; however, limited studies have demonstrated in situ imaging of nanoparticle assembly owing to the experimental challenges in controllably initiating and capturing ordering processes with single-particle resolution[29,30].

Here, using liquid-cell transmission electron microscopy (LCTEM)—an increasingly valuable technique for studying nanoscale dynamics of materials in their native environments[29,30,36–46]—we imaged the entire self-assembly pathways of gold nanocubes (AuNCs), a model shape-anisotropic nanocolloidal system, into diverse two-dimensional

[1]Department of Chemistry, Indiana University, Bloomington, IN, USA. [2]Department of Chemical Engineering, University of Michigan, Ann Arbor, MI, USA. [3]Biointerfaces Institute, University of Michigan, Ann Arbor, MI, USA. [4]These authors contributed equally: Yaxu Zhong, Timothy C. Moore, Tobias Dwyer. [✉]e-mail: sglotzer@umich.edu; xingchen@iu.edu
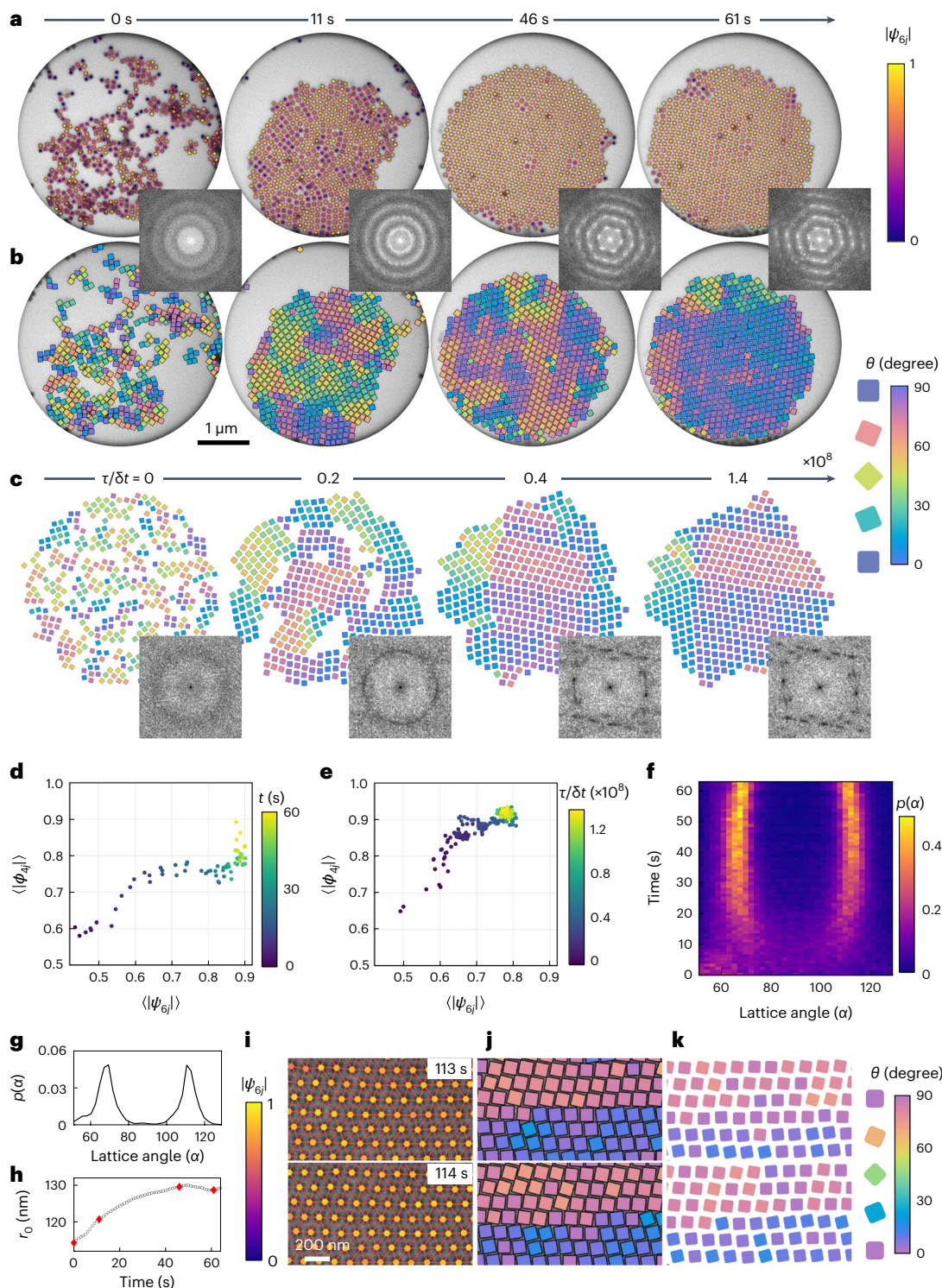
Fig. 1 | Charge screening controls the self-assembly phase behavior of gold nanocubes. a, LCTEM schematic showing the self-assembly of AuNCs near the Si₃N₄ windows under electron beam irradiation (gray cylinder) in organic solvent. **b**, Pairwise interaction potentials as a function of the center-to-center distance r_{CC} between AuNCs aligned face-to-face (schematic in inset), as used in the CG model (solid lines) or calculated from analytical theory (dashed line). Electr., electrostatic; an., analytical theory. **c**, Interaction potential fields $u(x, y)$ for a pair of parallel-aligned Au nanocubes assuming a total charge of 350 e⁻ per nanocube and screening lengths of 6 nm, 10 nm and 12 nm from left to right. The dark squares at the centers represent a single nanocube, whereas the lighter squares represent the excluded volume between the nanocubes. **d**, Schematic of the offset order parameter O_L used to characterize how square-like a lattice is. **e**, Schematics of the 2D superlattices observed experimentally. From left to right: SQ, RB and HR phases, corresponding to the $u(x, y)$ in **c**. **f**, Theoretical phase

diagram as a function of charge per nanocube (Q) and electrostatic screening length (λ). The background colors denote predicted phases characterized by O_L from the scaling theory, and the markers indicate structures observed in simulations at each (Q, λ) pair, colored by O_L. The black lines are contours of constant O_L that match the experimentally observed O_L for each lattice type. The blue line is the predicted loci of the RB-to-HR structural transition. **g–l**, Snapshots from simulations (**g**, **i** and **k**) and LCTEM experiments (**h**, **j** and **l**) with particles colored according to O_L with the same color map as in **f**. Gray particles have fewer than three nearest neighbors and were excluded from the O_L calculation. The insets are fast Fourier transform (FFT) patterns of a subregion of the image to highlight the symmetry of a single-crystalline grain. Simulation parameters (solvent conditions) are indicated above each simulation (experimental) snapshot. Sim, simulation; Exp, experiment.

(2D) superlattices. The dominant forces between AuNCs in solution include van der Waals (vdW) attractions and screened electrostatic repulsions given that AuNCs typically become charged under LCTEM imaging conditions (Fig. 1a)[30,47–49]. Previous work demonstrated that the electrostatic repulsion between nanoparticles decreases with increasing solvent polarity under LCTEM illumination, plausibly caused by higher ionic strength (resulting in a smaller screening length)

from solvent radiolysis[30]. Based on this observation and the fact that the solvent changes the vdW attractions to a negligible extent, we hypothesized that we can fine-tune the interaction potential between AuNCs and, hence, engineer their assembly behavior by varying the solvent. We performed molecular dynamics (MD) simulations of AuNC assembly explicitly accounting for these interactions and developed a scaling theory to show that the electrostatic screening controls the

Fig. 2 | Self-assembly pathway of gold nanocubes into the RB lattice.
a,b, Time-lapse LCTEM images and corresponding FFT patterns with nanocube centroids colored according to the modulus of sixfold bond-orientational order parameter ($|\psi_{6j}|$) and all nearest-neighbors connected (**a**), and nanocubes colored according to their orientations (**b**). **c**, Simulation snapshots and corresponding FFT patterns for the disorder-to-order transition of AuNCs into the RB lattice. **d,e**, Plots of averaged local translational and orientational order parameters ($\langle|\psi_{6j}|\rangle$, $\langle|\phi_{4j}|\rangle$) versus time for experimental LCTEM (**d**) and simulation (**e**) trajectories. **f**, Time-dependent lattice angle distribution from LCTEM experiment. **g**, Plot of lattice angle distribution of the RB phase at $t = 61$ s. **h**, Plot of nearest-neighbor distance retrieved from the first peak of $g(r)$ versus time. The red dots highlight the four stages shown in **a** and **b**. **i**–**k**, Movement of twin boundary through collective particle rotations in a nanocube superlattice. LCTEM images with nanocube centroids colored according to $|\psi_{6j}|$ (**i**). LCTEM images (**j**) and simulation snapshots (**k**) with nanocubes colored according to their orientations.

assembly behavior of these nanocubes. We quantified the pathways by analyzing the development of lattice translational order and particle orientational order during the assembly of AuNCs with solvent-tuned interparticle interactions, ranging from weakly to strongly attractive. Finally, we elucidated the pathways of superlattice melting and symmetry transitions, both induced by rapid solvent exchange.

Results

Theory and simulations of gold nanocube self-assembly

We developed a coarse-grained (CG) model to calculate the pairwise interactions between AuNCs (Supplementary Note 1 and Supplementary Fig. 1). We simulated systems over a range of electrostatic screening length (λ) and total charge (Q) based on estimates from our previous study[30]. As shown in Fig. 1b,c and Supplementary Fig. 2, the maximum overall attraction between AuNCs falls in the range of 5–40 kT. The interaction field becomes more isotropic and the effective particle size increases (considering a contour of zero potential) with increasing λ (Fig. 1c). Three ordered phases self-assembled from initial disorder in simulations, namely square-like (SQ), rhombic (RB) and hexagonal rotator (HR) phases, with increasing Q and λ (Fig. 1e,f and Supplementary Movies 1–3). We defined an offset-length order parameter O_L to quantify the extent to which these superlattices deviate from a perfect square lattice (Fig. 1d). With decreasing overall attraction (that is, increasing Q and λ), we observed increasing O_L values concomitant with the SQ-to-RB-to-HR symmetry transitions (Fig. 1f–l). These simulation results were insensitive to the charge distribution on the AuNCs (Supplementary Note 2 and Supplementary Fig. 3), suggesting that the predicted phase behavior is robust toward modest changes in the form of electrostatic repulsion between AuNCs. Moreover, we found the $O_L(Q, \lambda)$ relationships predicted by simulation collapse onto a master curve within a scaling theory (Supplementary Note 3 and Supplementary Fig. 3); this convergence indicates a universal relationship between interparticle interactions and the observed phase behavior. The scaling theory additionally enables identification of (Q, λ) pairs that yield the experimentally observed O_L values (Fig. 1f, black lines). Notably, there are no λ values that yield all three experimental O_L values across the range of Q studied, whereas all experimental O_L values are accessible by changing λ for $Q \geq 350$ e$^-$, suggesting that λ is the more relevant control variable of self-assembly behavior. Further, the stability limit of the HR phase can be estimated by assuming that it can be stable only when the center-to-center distance between AuNCs that minimizes the interaction potential (r_{min}) is such that AuNCs can rotate freely without colliding with nearest neighbors ($r_{min} > r^*$); we take r^* to be the sum of λ and the AuNC circumsphere diameter (Supplementary Note 4). Above (below) this stability limit (Fig. 1f, blue line), the HR phase is accessible (inaccessible) across the entire range of Q examined.
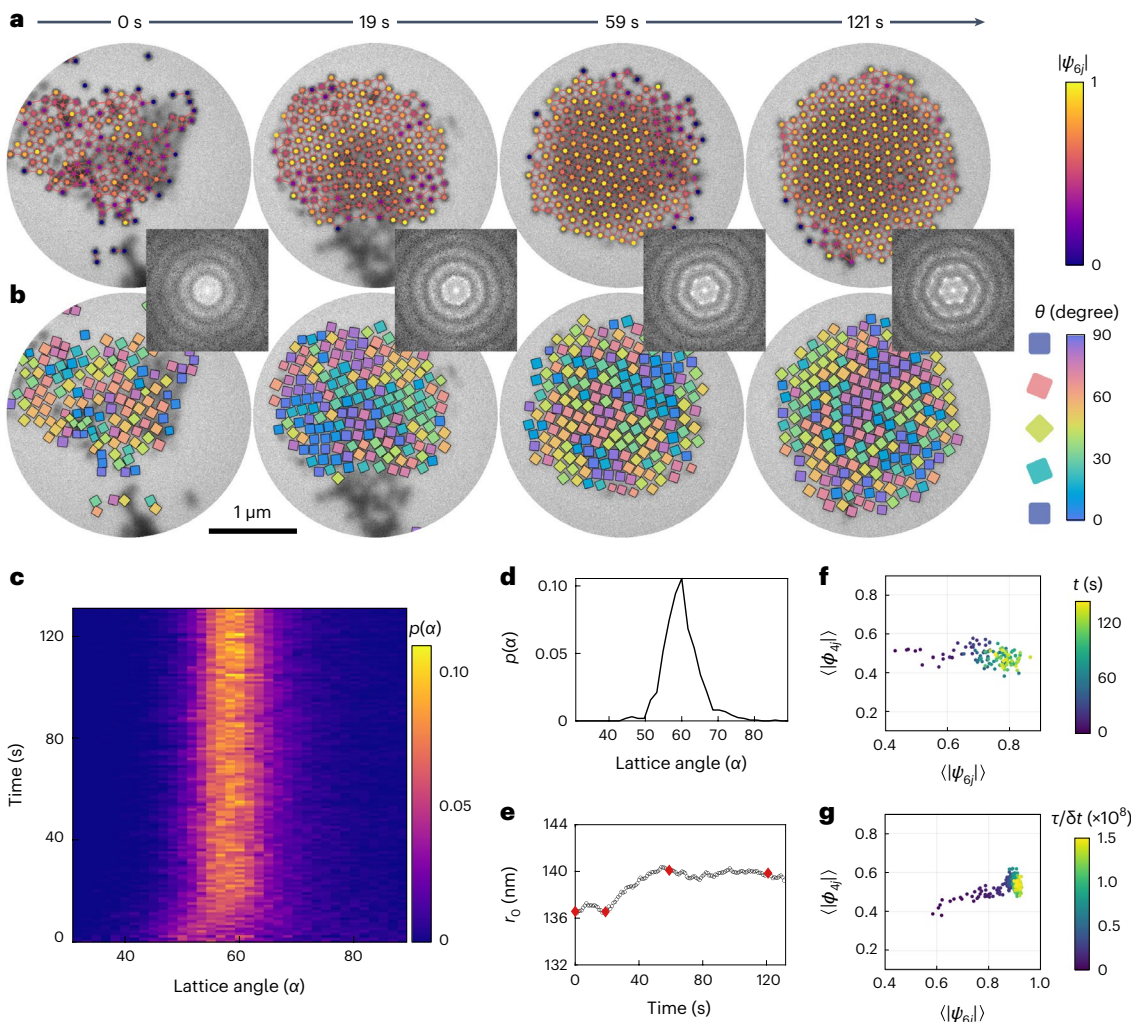
### Direct imaging and pathway analysis of gold nanocube self-assembly

We imaged the assembly process of polymer-grafted AuNCs into 2D superlattices in nonaqueous media using LCTEM (Fig. 1a). AuNCs (edge length $L_c = 87.4 \pm 3.2$ nm; Supplementary Fig. 4 and Supplementary Note 5) were densely grafted with thiol-terminated polystyrene (molecular weight $M_w = 3.2$ kDa) via ligand exchange to prevent uncontrolled aggregation under LCTEM conditions. The AuNCs became immobilized on the Si_3N_4 windows before transmission electron microscopy (TEM) imaging but began to move within seconds of electron beam illumination. The increased mobility is plausibly caused by positive charging of the AuNCs via contact electrification[47] or emission of Auger and secondary electrons[48–50] and positive charging of the Si_3N_4 windows[30,47,51,52]. With decreasing solvent polarity (butanol, 1:1 v/v octane/butanol and 4:1 v/v octane/butanol), we observed the formation of SQ, RB and HR phases, respectively, as indicated visually and by the fast Fourier transform (FFT) patterns of the TEM images, consistent with

simulations at $\lambda = 6$, 10 and 12 nm with $Q = 350$ e$^-$ (Fig. 1g–l). We also observed an increasing O_L with decreasing solvent polarity, analogous to the trend of increasing O_L with increasing screening length in simulations. The perimeters of the RB and HR phases are more dynamic than in the SQ phase, indicative of weaker net interparticle attraction in less polar solvents (cf. Supplementary Movies 4, 6 and 7). These computational and experimental results demonstrate that the interplay between vdW and electrostatic forces mediated by solvent polarity dictates the self-assembly phase behaviors of AuNCs. Our LCTEM imaging also allowed us to rule out interactions between polymer brushes as a driver of the self-assembly behaviors (Supplementary Notes 6 and 7).

Beyond characterizing the final structures, our LCTEM workflow enabled imaging and analysis of the full assembly pathways of AuNCs into superlattices (Supplementary Notes 8–10 and Supplementary Figs. 5–7). Figure 2a and Supplementary Movie 4 illustrate the four key stages during the formation of the RB phase. At 0 s, AuNCs were sparsely distributed within the field of view and exhibited low sixfold bond-orientational order ($\langle|\psi_{6j}|\rangle < 0.5$). The absence of long-range translational symmetry and AuNC orientational order were manifested by the diffuse rings of the corresponding FFT pattern and orientation plot (Fig. 2b), respectively. At 11 s, small hexagonally ordered domains exhibiting local facet alignment emerged. These domains were separated by disordered regions causing a lack of global translational order as shown by the FFT pattern. At 46 s, an extended 2D superlattice appeared. Despite its high sixfold bond-orientational order ($\langle|\psi_{6j}|\rangle > 0.7$), the corresponding AuNC orientation map revealed differently oriented domains each characterized by extensive facet alignment. At 61 s, a large coherent superlattice with extensive facet alignment had formed.

The evolution of the translational symmetry and orientational order during RB superlattice formation reveals an intriguing assembly pathway (Fig. 2d). From 0 to 11 s, both order parameters increased rapidly as individual AuNCs coalesced into a polycrystalline structure with short-range order. From 11 to 46 s, $\langle|\psi_{6j}|\rangle$ continually increased and the distribution of $|\psi_{6j}|$ narrowed drastically, whereas $\langle|\phi_{4j}|\rangle$ remained essentially constant and broadly distributed (Fig. 2d and Supplementary Fig. 8). These results indicate that the development of long-range translational order preceded extensive orientational order as the system eliminated grain boundaries and grew by adding AuNCs into the existing lattice. From 46 to 61 s, $\langle|\phi_{4j}|\rangle$ rose sharply. In essence, the rotational ordering of AuNCs through facet alignment induced a hexagonal-to-RB lattice transition. Such weak correlations between the two order parameters signify a nonclassical crystallization pathway where the interplay between nanocrystal shape and interaction at different densities gives rise to complex assembly dynamics. Remarkably, our simulation reproduced the nonclassical nature of the experimental self-assembly pathway (Fig. 2c,e). The symmetry transitions were further analyzed by calculating lattice angle distributions (Fig. 2f)[33,35,53,54]. From 10 to 40 s, two peaks near 60° and 120° were found, which indicates a hexagonal lattice. Afterward, the distributions shifted gradually toward 70° as the system evolved into the RB phase (Fig. 2f,g). The appearance of a shoulder next to the first peak in the pair distribution function $g(r)$ provides further evidence of the hexagonal-to-RB transition (Supplementary Fig. 8). The average nearest-neighbor distance gradually increased in the early stage, probably due to charge accumulation, and later stabilized as the system transitioned into the RB phase with increasing density (Fig. 2h). Intriguingly, AuNCs at twin boundaries can collectively rotate while maintaining high local translational order, which allowed the boundary to readily propagate through misaligned grains (Fig. 2i,j, Supplementary Fig. 9 and Supplementary Movie 5). We attribute this twin-boundary migration mode to the favorable energetics of facet alignment between adjacent AuNCs, which is reproduced in simulations (Fig. 2k). The ability to resolve boundaries through cooperative rearrangement of AuNCs during

Fig. 3 | Self-assembly pathway of gold nanocubes into the HR lattice.
a,b, Time-lapse LCTEM images and corresponding FFT patterns with nanocube centroids colored according to $|\psi_{6j}|$ (**a**) and nanocubes colored according to their orientations (**b**). **c**, Time-dependent lattice angle distribution. **d**, Plot of lattice angle distribution of the HR phase at $t = 121$ s. **e**, Plot of nearest-neighbor distance retrieved from the first peak of $g(r)$ versus time. The red dots highlight the four stages shown in **a** and **b**. **f,g**, Plots of averaged local translational and orientational order parameters ($\langle|\psi_{6j}|\rangle$, $\langle|\phi_{4j}|\rangle$) versus time from LCTEM (**f**) and simulation (**g**) data.
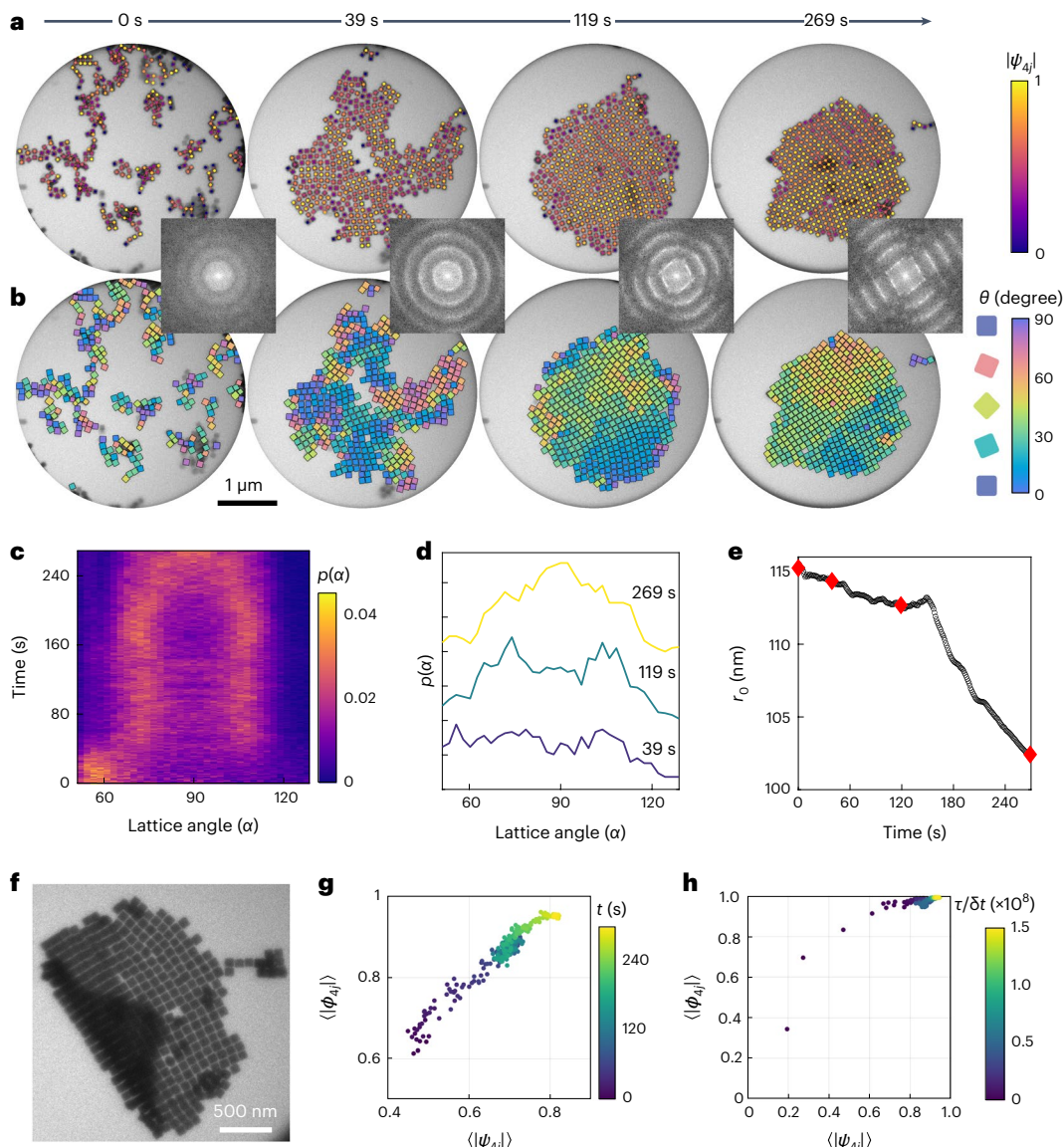
disorder-to-order transitions facilitates the formation of a single-crystalline RB superlattice.

The development of translational and orientational order during crystallization of the HR phase displayed a distinct pathway from the RB phase (Fig. 3 and Supplementary Movie 6). From 0 to 19 s, AuNCs assembled into a single domain consisting of a few hexagonally ordered subregions (Fig. 3a). These hexagonal regions continued to grow over the next 100 s to yield a coherent hexagonal superlattice, as illustrated by the transition from diffuse rings into sharp diffraction spots on the FFT patterns. Notably, orientational correlations among AuNCs remained short-ranged even after long-range translational order had developed, signifying the formation of a HR phase free of twin boundaries (Fig. 3b). The lattice angle distribution stayed narrowly distributed with the average close to 60° throughout the assembly process (Fig. 3c,d). The mean nearest-neighbor distance stabilized at around 140 nm after the initial rise (Fig. 3e). Notably, this value exceeds the circumdiameter of AuNCs suggesting that they can rotate freely. The decoupling of orientational and translational order was further quantified through analysis of the order parameters $\langle|\psi_{6j}|\rangle$ and $\langle|\phi_{4j}|\rangle$ (Fig. 3f and Supplementary Fig. 10). As $|\psi_{6j}|$ gradually increased and narrowed, $|\phi_{4j}|$ remained widely distributed with $\langle|\phi_{4j}|\rangle \approx 0.5$, confirming the low

orientational order observed visually. The HR phase remained intact for several minutes under electron-beam illumination, suggesting that it is the stable phase under such conditions. The simulation at $(Q, \lambda) = (350\ e^-, 12\ nm)$ uncovered a similar kinetic pathway featuring decoupled evolution of translational and orientational order (Fig. 3g). This agreement indicates that our CG model captures the underlying physics of the experimental system.

We further examined the assembly pathway of AuNCs in high-polarity solvent (Fig. 4 and Supplementary Movie 7). Here, we used ψ_{4j} rather than ψ_{6j} to analyze local translational order, as ψ_{4j} better quantifies the SQ order observed experimentally (Fig. 4a)[54]. From 0 to 39 s, an extended network of SQ domains developed as AuNCs diffused and interacted with each other. At 119 s, a single grain consisting of extended SQ subdomains had formed, as indicated by four sets of wide FFT peaks separated by ~90°. From 119 to 269 s, SQ regions continued to enlarge resulting in narrower Bragg peaks in the FFT pattern. The lattice angles initially exhibited bimodal distributions and later merged into a single broad distribution centered at about 90° (Fig. 4c,d). Importantly, many lattice angles close to 90° were already seen at ~40 s, suggesting that there existed a tendency to maximize local facet alignment among AuNCs since the early stage of assembly. The temporal evolution of

**Fig. 4 | Self-assembly pathway of gold nanocubes into the SQ lattice.**
a,b, Time-lapse LCTEM images and corresponding FFT patterns with nanocube centroids colored according to $|\psi_{4j}|$ (**a**) and nanocubes colored according to their orientations (**b**). **c**, Time-dependent lattice angle distribution. **d**, Plots of lattice angle distribution corresponding to the final three LCTEM images in **a** and **b**. **e**, Plot of nearest-neighbor distance retrieved from the first peak of $g(r)$ versus time.
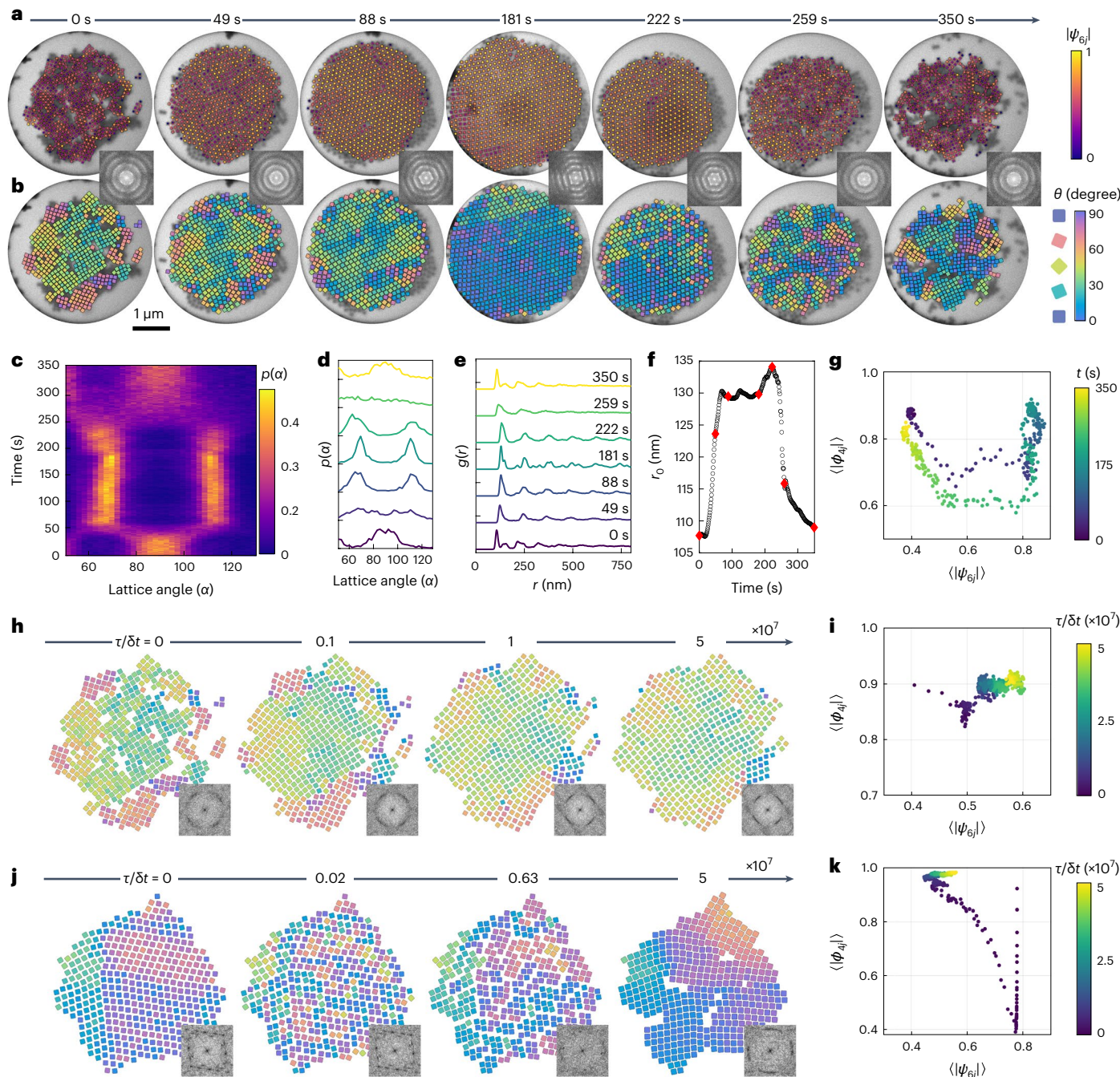
The red dots highlight the four stages shown in **a** and **b**. **f**, LCTEM image showing the detachment of the SQ nanocube superlattice from the Si_3N_4 window after prolonged exposure to the electron beam. **g,h**, Plots of averaged local translational and orientational order parameters order parameters ($\langle|\psi_{6j}|\rangle$, $\langle|\phi_{4j}|\rangle$) versus time for LCTEM (**g**) and simulation (**h**) trajectories.

$g(r)$ reveals the development of long-range SQ order as high-order peaks gradually intensified (Supplementary Fig. 11). The average nearest-neighbor spacing monotonically decreased during assembly and reached ~102 nm at 269 s (Fig. 4e). AuNC rotation became restricted at this short distance and the superlattice continued to densify owing to strong interparticle attraction. Eventually, the superlattice membrane peeled away from the Si_3N_4 window (Fig. 4f, Supplementary Fig. 12 and Supplementary Movie 8), which is indicative of the mechanical strength provided by the strong vdW attraction and possibly the onset of polymer brush interpenetration at short distances. Distinct from the RB and HR phases, $\langle|\phi_{4j}|\rangle$ and $\langle|\psi_{4j}|\rangle$ increased concurrently and their distributions gradually narrowed during crystallization (Fig. 4g and Supplementary Fig. 11). Such enhanced coupling between translational and orientational order, which is reproduced by simulation (Fig. 4h), is attributed to strong attraction between AuNCs in high-polarity solvent and explains the absence of a 'square rotator' phase.

The dynamic nature of the superlattices allowed visualization of defect generation and migration. For all three phases, rows of AuNCs collectively shifted along the symmetry axes of the lattice to fill vacancies (Supplementary Figs. 13–15 and Supplementary Movie 9), as also observed in simulations (Supplementary Movies 1–3). Further, the experimental SQ lattice displayed vacancy generation and migration via a hopping mechanism. Here, vacancies formed spontaneously and translated stepwise along the symmetry axes of the lattice, occasionally oscillating between neighboring lattice sites, and vanished after reaching the periphery (Supplementary Fig. 13 and Supplementary Movie 9). This hopping mode resulted in lower vacancy mobilities compared with the RB and HR phase, indicating stronger net attractions between AuNCs forming the SQ phase[55]. Altogether, the similarities between experiment and simulation demonstrate that the interactions between AuNCs play a key role in controlling not only assembly pathways but also the defect dynamics within the superlattices.

Fig. 5 | Solvent-mediated, reversible structural transitions between the SQ and the RB phases. a,b, Time-lapse LCTEM images and corresponding FFT patterns with nanocube centroids colored according to $|\psi_{6j}|$ (**a**) and nanocubes colored according to their orientations (**b**). **c**, Time-dependent lattice angle distribution. **d,e**, Plots of lattice angle distribution (**d**) and $g(r)$ (**e**) corresponding to the LCTEM images in **a** and **b**. **f**, Plot of nearest-neighbor distance retrieved from the first peak of $g(r)$ versus time. The red dots highlight the seven snapshots shown in **a** and **b**. **g**, Plot of averaged local order parameters ($\langle|\psi_{6j}|\rangle$, $\langle|\phi_{4j}|\rangle$) versus time for the LCTEM trajectory. **h–k**, Simulation snapshots with inset FFT patterns (**h** and **j**) and corresponding plots of averaged local translational and orientational order parameters ($\langle|\psi_{6j}|\rangle$, $\langle|\phi_{4j}|\rangle$) versus time for the SQ-to-RB lattice transition (**h** and **i**) and vice versa (**j** and **k**).

Solvent-mediated structural transitions between distinct superlattices

Having elucidated the self-assembly pathways of AuNCs in different solvents, we further explored superlattice reconfiguration with LCTEM and simulations. Starting from a multi-grain SQ lattice formed in butanol, we triggered its reconfiguration by quickly changing the solvent to a medium-polarity one (octane:butanol 1:1 (v/v)) and later back to butanol (Fig. 5, Supplementary Figs. 16 and 17 and Supplementary Movie 10). An extended RB superlattice emerged as indicated by the

sharp spots in the FFT pattern, which subsequently returned to the polycrystalline SQ lattice (Fig. 5a,b). Lattice angle analyses revealed a fast switch from single broad distributions centered at 90° to bimodal distributions at ~50 s, which is consistent with the development of multiple RB domains as seen from LCTEM (Fig. 5c,d). Analysis of $g(r)$ provided further evidence of the SQ-to-RB transition by showing that the nearest-neighbor distance gradually increased as the RB lattice was forming (Fig. 5e,f). Initially, $\langle|\phi_{4j}|\rangle$ decreased while $\langle|\psi_{6j}|\rangle$ increased. Afterward, $\langle|\phi_{4j}|\rangle$ essentially plateaued and $\langle|\psi_{6j}|\rangle$ continued to rise

followed by a steep increase in $\langle|\phi_{4j}|\rangle$ (Fig. 5g). Despite different starting states, the pathway after the initial drop in $\langle|\phi_{4j}|\rangle$ showed good agreement with that of the RB lattice formation from disorder (cf. Fig. 2c). We observed a similar but less pronounced initial decrease in $\langle|\phi_{4j}|\rangle$ in simulation, after which $\langle|\phi_{4j}|\rangle$ and $\langle|\psi_{6j}|\rangle$ increased simultaneously (Fig. 5h,i and Supplementary Movie 11). The RB-to-SQ transition, on the other hand, involved a HR-like intermediate. After solvent replacement at ~180 s, we observed a rapid decline in orientational order before the loss of lattice translational order (Fig. 5f,g), as also found in the RB-to-SQ simulation (Fig. 5j,k and Supplementary Movie 12). The appearance of HR-like intermediates probably arises from a smaller effective size of AuNCs and, hence, local particle density upon changing to a more polar solvent (Fig. 1c). The enhanced AuNC rotational freedom apparently facilitated subsequent transition to the SQ lattice. A similar fast drop in orientational order was also observed during melting of the RB lattice (Supplementary Figs. 18 and 19 and Supplementary Movie 13), which we attribute to the more isotropic and weakened interactions after switching to the low-polarity solvent (Supplementary Fig. 2). Occasionally, we also observed a different pathway for the RB-to-SQ transition in LCTEM that involved lattice distortion through collective rotation of AuNCs (Supplementary Fig. 20 and Supplementary Movie 14). The actual pathway that the system selects may depend on the local density of AuNCs and concentration of vacancies, with denser and defect-free grains probably favoring a diffusionless pathway. The solvent-mediated transitions between the SQ and RB phases appeared to be reversible based upon the nearly overlapping U-shaped trajectory of the system in ($\langle|\psi_{6j}|\rangle$, $\langle|\phi_{4j}|\rangle$) space (Fig. 5g).

Discussion

In this work, we demonstrate a versatile strategy to engineer self-assembly pathways for shape-anisotropic nanoparticles while visualizing the complete assembly process using LCTEM imaging. By controlling the solvent environment, we were able to direct the formation of a HR phase with translational order but orientational disorder for weakly attractive AuNCs, and RB and SQ phases from increasingly attractive AuNCs. Using MD simulations and scaling theory, we showed that the balance between vdW attraction and electrostatic repulsion in different solvents controls superlattice formation. In both LCTEM and simulation, the evolution of lattice translational order and particle orientational order were largely decoupled during the assembly of the HR phase and strongly coupled during the assembly of the SQ phase, whereas the degree of coupling varied at different stages of the assembly process of the RB phase. Next, we expanded the capability of LCTEM to study solid–solid transitions triggered by in situ rapid solvent exchange. We observed a HR-like intermediate during the RB-to-SQ transition, and our simulations illustrated that the decreased effective particle size due to the change in electrostatic screening facilitates the formation of this intermediate. The agreement between theory, simulation and experiment provides a robust, predictive framework for understanding and manipulating assembly pathways, and we expect our findings to be applicable to a wide variety of nanocolloidal systems, regardless of the origin of their interactions. Our joint experiment–simulation–theory study thereby opens new avenues for the bottom-up design of responsive and adaptive materials-on-demand by engineering the building block attributes, kinetic assembly pathways and superlattice structure in self-assembling nanocolloids.

Methods

Computational model of AuNC and MD simulations

We modeled the AuNCs as a 2D rigid body of point particles by discretizing the particles into two types of interaction sites: a series of sites around the perimeter of the body that interact through a Yukawa potential and a grid of sites that span the body of the particle and interact through a Mie potential. The Yukawa and Mie potentials represent the screened electrostatic and Au–Au vdW interactions, respectively.

MD simulations were executed with HOOMD-Blue[56]. Further details of the model parameterization and MD simulations are provided in Supplementary Note 1.

Synthesis and characterization of polystyrene-grafted AuNCs

AuNCs were synthesized via iterative reductive growth and oxidative dissolution reactions based on a previously reported method with modifications[57]. To prepare polystyrene-grafted AuNCs, 0.5 ml of the pristine AuNC solution was first concentrated to ~100 μl via centrifugation at 1,540 × g for 3 min. Next, this concentrated solution was added dropwise into a 10 ml tetrahydrofuran (THF) solution (2 mg ml⁻¹) of thiol-terminated polystyrene (M_w = 3.2 kDa) under sonication. The resultant mixture was left undisturbed for 24 h at room temperature. Afterward, the polystyrene-grafted AuNCs were purified via three rounds of centrifugation at 2,740 × g for 3 min, each time followed by redispersion into 3 ml of THF. After the last centrifugation step, the polystyrene-grafted AuNCs were dispersed in 200 μl of THF for LCTEM experiments. Low-magnification TEM images were recorded on a JEOL JEM-1400plus electron microscope with a LaB₆ filament operating at 120 kV. TEM samples were prepared by drop-casting ~10 μl of AuNC solution onto 300-mesh carbon-coated copper grids (Ted Pella). Scanning electron microscopy (SEM) images were taken on a Carl Zeiss Auriga 60 FIB-SEM operated at 1.50 kV. Further details on nanocrystal synthesis are provided in Supplementary Note 5.

In situ LCTEM imaging

In situ LCTEM imaging was performed on a JEOL JEM-1400plus electron microscope using a Protochips Poseidon Select holder. Bottom E-chips with a 150 nm integrated gold spacer (EPB-52DF-10) and top E-chips with the nominal window dimension of 550 μm × 20 μm (EPT-52W-10) were used in all experiments. LCTEM movies were recorded by a Gatan OneView CMOS camera with 4096 × 4096 pixels at a frame rate of 5 fps. Further details on LCTEM imaging and image processing and analysis are provided in Supplementary Notes 8–10.

Data availability

The source data for the figures in the main text are available in Supplementary Information.

References

1. Libbrecht, K. G. The physics of snow crystals. *Rep. Prog. Phys.* **68**, 855–895 (2005).
2. Sauter, A. et al. Real-time observation of nonclassical protein crystallization kinetics. *J. Am. Chem. Soc.* **137**, 1485–1491 (2015).
3. Pogatscher, S. et al. Solid–solid phase transitions via melting in metals. *Nat. Commun.* **7**, 11113 (2016).
4. De Yoreo, J. J. et al. Crystallization by particle attachment in synthetic, biogenic, and geologic environments. *Science* **349**, aaa6760 (2015).
5. Boles, M. A., Engel, M. & Talapin, D. V. Self-assembly of colloidal nanocrystals: from intricate structures to functional materials. *Chem. Rev.* **116**, 11220–11289 (2016).
6. Li, B., Zhou, D. & Han, Y. Assembly and phase transitions of colloidal crystals. *Nat. Rev. Mater.* **1**, 15011 (2016).
7. Ye, X. et al. Competition of shape and interaction patchiness for self-assembling nanoplates. *Nat. Chem.* **5**, 466–473 (2013).
8. Choi, J.-H. et al. Exploiting the colloidal nanocrystal library to construct electronic devices. *Science* **352**, 205–208 (2016).
9. Liu, W. et al. Diamond family of nanoparticle superlattices. *Science* **351**, 582–586 (2016).
10. Lin, H. et al. Clathrate colloidal crystals. *Science* **355**, 931–935 (2017).
11. Nagaoka, Y. et al. Superstructures generated from truncated tetrahedral quantum dots. *Nature* **561**, 378–382 (2018).
12. Alberstein, R., Suzuki, Y., Paesani, F. & Tezcan, F. A. Engineering the entropy-driven free-energy landscape of a dynamic nanoporous protein assembly. *Nat. Chem.* **10**, 732–739 (2018).

13. Bian, T. et al. Electrostatic co-assembly of nanoparticles with oppositely charged small molecules into static and dynamic superstructures. *Nat. Chem.* **13**, 940–949 (2021).
14. Santos, P. J. et al. Macroscopic materials assembled from nanoparticle superlattices. *Nature* **591**, 586–591 (2021).
15. Li, Z., Fan, Q. & Yin, Y. Colloidal self-assembly approaches to smart nanostructured materials. *Chem. Rev.* **122**, 4976–5067 (2022).
16. Coropceanu, I. et al. Self-assembly of nanocrystals into strongly electronically coupled all-inorganic supercrystals. *Science* **375**, 1422–1426 (2022).
17. Wang, Y. et al. Structural diversity in dimension-controlled assemblies of tetrahedral gold nanocrystals. *J. Am. Chem. Soc.* **144**, 13538–13546 (2022).
18. Han, H. et al. Multiscale hierarchical structures from a nanocluster mesophase. *Nat. Mater.* **21**, 518–525 (2022).
19. Kumar, P. et al. Photonically active bowtie nanoassemblies with chirality continuum. *Nature* **615**, 418–424 (2023).
20. Wang, Y. et al. Controlled self-assembly of gold nanotetrahedra into quasicrystals and complex periodic supracrystals. *J. Am. Chem. Soc.* **145**, 17902–17911 (2023).
21. Nguyen, Q. N. et al. Colloidal synthesis of metal nanocrystals: from asymmetrical growth to symmetry breaking. *Chem. Rev.* **123**, 3693–3760 (2023).
22. Silvera Batista, C. A., Larson, R. G. & Kotov, N. A. Nonadditivity of nanoparticle interactions. *Science* **350**, 1242477 (2015).
23. Král, P. et al. Simulation methods for self-assembling nanoparticles. *Prog. Mater. Sci.* **142**, 101225 (2024).
24. Waltmann, T., Waltmann, C., Horst, N. & Travesset, A. Many body effects and icosahedral order in superlattice self-assembly. *J. Am. Chem. Soc.* **140**, 8236–8245 (2018).
25. Lee, S., Teich, E. G., Engel, M. & Glotzer, S. C. Entropic colloidal crystallization pathways via fluid–fluid transitions and multidimensional prenucleation motifs. *Proc. Natl. Acad. Sci. USA* **116**, 14843–14851 (2019).
26. Zhang, T. H. & Liu, X. Y. How does a transient amorphous precursor template crystallization. *J. Am. Chem. Soc.* **129**, 13520–13526 (2007).
27. Savage, J. R. & Dinsmore, A. D. Experimental evidence for two-step nucleation in colloidal crystallization. *Phys. Rev. Lett.* **102**, 198302 (2009).
28. Peng, Y. et al. Two-step nucleation mechanism in solid–solid phase transitions. *Nat. Mater.* **14**, 101–108 (2015).
29. Ou, Z. et al. Kinetic pathways of crystallization at the nanoscale. *Nat. Mater.* **19**, 450–455 (2020).
30. Zhong, Y. et al. Multistep crystallization of dynamic nanoparticle superlattices in nonaqueous solutions. *J. Am. Chem. Soc.* **144**, 14915–14922 (2022).
31. Leunissen, M. E. et al. Ionic colloidal crystals of oppositely charged particles. *Nature* **437**, 235–240 (2005).
32. Sacanna, S., Irvine, W. T. M., Chaikin, P. M. & Pine, D. J. Lock and key colloids. *Nature* **464**, 575–578 (2010).
33. Zhao, K., Bruinsma, R. & Mason, T. G. Entropic crystal–crystal transitions of Brownian squares. *Proc. Natl Acad. Sci. USA* **108**, 2684–2687 (2011).
34. Shah, A. A. et al. Actuation of shape-memory colloidal fibres of Janus ellipsoids. *Nat. Mater.* **14**, 117–124 (2015).
35. Rossi, L. et al. Shape-sensitive crystallization in colloidal superball fluids. *Proc. Natl Acad. Sci. USA* **112**, 5286–5290 (2015).
36. Liao, H.-G. et al. Facet development during platinum nanocube growth. *Science* **345**, 916–919 (2014).
37. Ross, F. M. Opportunities and challenges in liquid cell electron microscopy. *Science* **350**, aaa9886 (2015).
38. Ye, X. et al. Single-particle mapping of nonequilibrium nanocrystal transformations. *Science* **354**, 874–877 (2016).
39. Sutter, E. et al. In situ microscopy of the self-assembly of branched nanocrystals in solution. *Nat. Commun.* **7**, 11213 (2016).
40. Lin, G. et al. Linker-mediated self-assembly dynamics of charged nanoparticles. *ACS Nano* **10**, 7443–7450 (2016).
41. Loh, N. D. et al. Multistep nucleation of nanocrystals in aqueous solution. *Nat. Chem.* **9**, 77–82 (2017).
42. Tan, S. F. et al. Nanoparticle interactions guided by shape-dependent hydrophobic forces. *Adv. Mater.* **30**, 1707077 (2018).
43. Ianiro, A. et al. Liquid–liquid phase separation during amphiphilic self-assembly. *Nat. Chem.* **11**, 320–328 (2019).
44. Song, M. et al. Oriented attachment induces fivefold twins by forming and decomposing high-energy grain boundaries. *Science* **367**, 40–45 (2020).
45. Kim, B. H. et al. Critical differences in 3D atomic structure of individual ligand-protected nanocrystals in solution. *Science* **368**, 60–67 (2020).
46. Yang, Y. et al. Operando studies reveal active Cu nanograins for CO_2 electroreduction. *Nature* **614**, 262–269 (2023).
47. Woehl, T. J. & Prozorov, T. The mechanisms for nanoparticle surface diffusion and chain self-assembly determined from real-time nanoscale kinetics in liquid. *J. Phys. Chem. C* **119**, 21261–21269 (2015).
48. Zheng, H., Mirsaidov, U. M., Wang, L.-W. & Matsudaira, P. Electron beam manipulation of nanoparticles. *Nano Lett.* **12**, 5644–5648 (2012).
49. White, E. R., Mecklenburg, M., Shevitski, B., Singer, S. B. & Regan, B. C. Charged nanoparticle dynamics in water induced by scanning transmission electron microscopy. *Langmuir* **28**, 3695–3698 (2012).
50. Woehl, T. J. et al. Experimental procedures to mitigate electron beam induced artifacts during in situ fluid imaging of nanomaterials. *Ultramicroscopy* **127**, 53–63 (2013).
51. Liu, Y., Lin, X. M., Sun, Y. & Rajh, T. In situ visualization of self-assembly of charged gold nanoparticles. *J. Am. Chem. Soc.* **135**, 3764–3767 (2013).
52. Chee, S. W. et al. Desorption-mediated motion of nanoparticles at the liquid–solid interface. *J. Phys. Chem. C* **120**, 20462–20470 (2016).
53. Avendaño, C. & Escobedo, F. A. Phase behavior of rounded hard-squares. *Soft Matter* **8**, 4675–4681 (2012).
54. Meijer, J.-M. et al. Convectively assembled monolayers of colloidal cubes: evidence of optimal packings. *Langmuir* **35**, 4946–4955 (2019).
55. van der Meer, B. et al. Revealing a vacancy analog of the crowdion interstitial in simple cubic crystals. *Phys. Rev. Lett.* **121**, 258001 (2018).
56. Anderson, J. A., Glaser, J. & Glotzer, S. C. Hoomd-blue: a Python package for high-performance molecular dynamics and hard particle Monte Carlo simulations. *Comput. Mater. Sci.* **173**, 109363 (2020).
57. O'Brien, M. N., Jones, M. R., Brown, K. A. & Mirkin, C. A. Universal noble metal nanoparticle seeds realized through iterative reductive growth and oxidative dissolution reactions. *J. Am. Chem. Soc.* **136**, 7603–7606 (2014).

Acknowledgements

Authors contributions

Y.Z. and X.Y. designed the experiments. Y.Z., Y.W. and F.C. performed the experiments. Y.Z., T.C.M., T.D., A.B.-G., V.R.A., J.C. and X.Y. analyzed the experimental data. T.C.M., T.D. and S.C.G. designed the theoretical model and performed the simulations. Y.Z., T.C.M, T.D., J.C., S.C.G. and X.Y. wrote the manuscript. S.C.G. and X.Y. supervised the project. All authors discussed the results and commented on the manuscript.

Competing interests

The authors declare no competing interests.

Additional information

Supplementary information The online version contains supplementary material available at https://doi.org/10.1038/s44286-024-00102-9.

Correspondence and requests for materials should be addressed to Sharon C. Glotzer or Xingchen Ye.

Peer review information *Nature Chemical Engineering* thanks Taylor Woehl, Petra Kral and Ethayaraja Mani for their contribution to the peer review of this work.

Reprints and permissions information is available at www.nature.com/reprints.

Engineering and direct imaging of nanocube self-assembly pathways

Table of Contents

Description of Supplementary Movies

Supplementary Movie 1. Computational self-assembly of gold nanocubes into a square-like lattice. Particles are colored by their orientations. The animation spans a simulation timescale of $8.7 \times 10^5 \, \tau$.

Supplementary Movie 2. Computational self-assembly of gold nanocubes into a rhombic lattice. Particles are colored by their orientations. The animation spans a simulation timescale of $1.38 \times 10^6 \, \tau$.

Supplementary Movie 3. Computational self-assembly of gold nanocubes into a hexagonal rotator phase. Particles are colored by their orientations. The animation spans a simulation timescale of $9.8 \times 10^5 \, \tau$.

Supplementary Movie 4. Self-assembly of gold nanocubes into the rhombic lattice. (a) Raw LCTEM movie. (b-d) LCTEM movie frames with nanocubes colored according to their orientations (b), nanocube centroids colored according to $|\psi_{6j}|$ and all nearest-neighbors connected (c), and nanocube centroids colored according to $|\phi_{4j}|$ (d). (e) Radial distribution function g(r) plots and (f) FFT patterns of LCTEM movie frames. (g) 2D scatter plots of the order parameters $|\psi_{6j}|$ and $|\phi_{4j}|$. (h) Plots of ensemble-averaged local translational and orientational order parameters $(\langle|\psi_{6j}|\rangle, \langle|\phi_{4j}|\rangle)$ versus time. Dose rate: 14.0 e⁻·Å⁻²·s⁻¹. The frame rates are 15 fps (15 times faster than real time).

Supplementary Movie 5. Movement of a twin boundary in the rhombic lattice through collective rotation of nanocubes. (top) LCTEM movie frames with nanocubes colored according to their orientations and (bottom) nanocube centroids colored according to $|\psi_{6j}|$. Dose rate: 14.0 e⁻·Å⁻²·s⁻¹. The frame rates are 5 fps (5 times faster than real time).

Supplementary Movie 6. Self-assembly of gold nanocubes into the hexagonal rotator lattice. (a) Raw LCTEM movie. (b-d) LCTEM movie frames with nanocubes colored according to their orientations (b), nanocube centroids colored according to $|\psi_{6j}|$ and all nearest-neighbors connected (c), and nanocube centroids colored according to $|\phi_{4j}|$ (d). (e) Radial distribution function g(r) plots and (f) FFT patterns of LCTEM movie frames. (g) 2D scatter plots of the order parameters $|\psi_{6j}|$ and $|\phi_{4j}|$. (h) Plots of ensemble-averaged local translational and orientational order parameters $(\langle|\psi_{6j}|\rangle, \langle|\phi_{4j}|\rangle)$ versus time. Dose rate: 14.0 e⁻·Å⁻²·s⁻¹. The frame rates are 15 fps (15 times faster than real time).

Supplementary Movie 7. Self-assembly of gold nanocubes into the square-like lattice. (a) Raw LCTEM movie. (b-d) LCTEM movie frames with nanocubes colored according to their orientations (b), nanocube centroids colored according to $|\psi_{4j}|$ and all nearest-neighbors connected (c), and nanocube centroids colored according to $|\phi_{4j}|$ (d). (e) Radial distribution function g(r) plots and (f) FFT patterns of LCTEM movie frames. (g) 2D scatter plots of the order parameters $|\psi_{4j}|$ and $|\phi_{4j}|$. (h) Plots of ensemble-averaged local translational and orientational order parameters $(\langle|\psi_{4j}|\rangle, \langle|\phi_{4j}|\rangle)$ versus time. Dose rate: 14.0 e⁻·Å⁻²·s⁻¹. The frame rates are 15 fps (15 times faster than real time).

Supplementary Movie 8. Detachment of the square-like superlattice from the Si$_3$N$_4$ window. Dose rate: 14.0 e$^-$·Å^{-2}·s^{-1}. The frame rates are 15 fps (15 times faster than real time).

Supplementary Movie 9. Vacancy formation and vacancy removal pathways for the hexagonal rotator, rhombic and square-like superlattices. Dose rate: 14.0 e$^-$·Å^{-2}·s^{-1} for all three movies. The frame rates are 5 fps (real time).

Supplementary Movie 10. Solvent-mediated reversible structural transitions between the square-like and the rhombic phases. (a) Raw LCTEM movie. (b-d) LCTEM movie frames with nanocubes colored according to their orientations (b), nanocube centroids colored according to $|\psi_{6j}|$ and all nearest-neighbors connected (c), and nanocube centroids colored according to $|\phi_{4j}|$ (d). (e) Radial distribution function g(r) plots and (f) FFT patterns of LCTEM movie frames. (g) 2D scatter plots of the order parameters $|\psi_{6j}|$ and $|\phi_{4j}|$. (h) Plots of ensemble-averaged local translational and orientational order parameters $(\langle|\psi_{6j}|\rangle, \langle|\phi_{4j}|\rangle)$ versus time. Dose rate: 14.0 e$^-$·Å^{-2}·s^{-1}. The frame rates are 15 fps (15 times faster than real time).

Supplementary Movie 11. Simulated structural transition from the square-like lattice to the rhombic lattice induced by a change in the screening length. Particles are colored by their orientations. The animation spans a simulation timescale of $2.0 \times 10^5 \, \tau$.

Supplementary Movie 12. Simulated structural transition from the rhombic lattice to the square-like lattice induced by a change in the screening length. Particles are colored by their orientations. The animation spans a simulation timescale of $2.0 \times 10^5 \, \tau$. Note that the time period between snapshots is not constant throughout the movie; the period between snapshots is $\tau/\delta t = 10$ when $\tau/\delta t > 1{,}000$, $10{,}000$ when $1{,}000 \le \tau/\delta t < 1 \times 10^6$, and $50{,}000$ when $\tau/\delta t \ge 1 \times 10^6$.

Supplementary Movie 13. Melting of the rhombic lattice induced by changing the solvent from medium-polarity (1:1 v/v octane/butanol) to low-polarity one (4:1 v/v octane/butanol). (a) Raw LCTEM movie. (b-d) LCTEM movie frames with nanocubes colored according to their orientations (b), nanocube centroids colored according to $|\psi_{6j}|$ and all nearest-neighbors connected (c), and nanocube centroids colored according to $|\phi_{4j}|$ (d). (e) Radial distribution function g(r) plots and (f) FFT patterns of LCTEM movie frames. (g) 2D scatter plots of the order parameters $|\psi_{6j}|$ and $|\phi_{4j}|$. (h) Plots of ensemble-averaged local translational and orientational order parameters $(\langle|\psi_{6j}|\rangle, \langle|\phi_{4j}|\rangle)$ versus time. Dose rate: 14.0 e$^-$·Å^{-2}·s^{-1}. The frame rates are 15 fps (15 times faster than real time).

Supplementary Movie 14. Structural transition from the square-like to the rhombic lattice induced by changing the solvent from high-polarity (butanol) to medium-polarity one (1:1 v/v octane/butanol). A different pathway from the one shown in Figure 5 was observed which involved continuous lattice distortion through collective rotation of AuNCs without losing orientational order. Dose rate: 14.0 e$^-$·Å^{-2}·s^{-1}. The frame rates are 15 fps (15 times faster than real time).

Supplementary Notes

Supplementary Note 1. Description of molecular dynamics model and method

Coarse-grained molecular dynamics model and parameterization. We developed a coarse-grained (CG) model to calculate the pairwise interaction potentials between AuNCs and to probe their assembly behavior, both as a function of the electrostatic screening length of the solvent. Given the strong adsorption of AuNCs to the Si_3N_4 membrane in LCTEM experiments, pair configurations have three degrees of freedom (one for the interparticle separation and one for the orientation of each particle), allowing us to model the AuNCs as a two-dimensional (2D) system of anisotropic particles (i.e., as rounded squares).

Our model consists of two types of interaction sites $\{s_{el}\}$ and $\{s_{vdW}\}$ to account for the screened electrostatic repulsion and van der Waals (vdW) attraction between AuNCs, respectively. Since the AuNCs are electrically conductive, the charges migrate to the surface, so we place s_{el} sites equally spaced around the perimeter of the rounded square (Supplementary Fig. 1). We assign a charge to each $s_{el}^{(i)} \in \{s_{el}\}$ based on three factors: (1) its location on the perimeter, (2) the total particle charge Q, and (3) the *charge asymmetry factor* f_{CA}. When $f_{CA} = 1$, each site gets a charge equal to $Q/|\{s_{el}\}|$, where $|\{s_{el}\}|$ is the number of electrostatic interaction sites. When $f_{CA} \neq 1$, each corner bead is assigned a charge f_{CA} times the charge on each of the non-corner beads, still with the constraint that the total charge is Q. All sites $\{s_{el}\}$ on each particle interact with all sites $\{s_{el}\}$ on neighboring particles through a Yukawa potential of the form

$$u_{el}(r_{ij}) = \frac{Q_i Q_j}{4\pi \varepsilon_r \varepsilon_0} \cdot \frac{e^{\frac{-r_{ij}}{\lambda}}}{r_{ij}},$$

where Q_i is the charge on $s_{el}^{(i)}$, ε_r is the relative permittivity of the solvent (7.74),[1] ε_0 is the vacuum permittivity, and λ is the electrostatic screening length of the solvent (a parameter of the model).

The sites $\{s_{vdW}\}$ sit on a 3x3 grid centered in the rounded square and interact pairwise with all $s_{vdW}^{(i)}$ on neighboring particles through a Mie potential of the form

$$u_{vdW}(r_{ij}) = \left(\frac{n}{n-m}\right)\left(\frac{n}{m}\right)^{\frac{m}{n-m}} \varepsilon_{vdW} \left[\left(\frac{\sigma_{vdW}}{r_{ij}}\right)^n - \left(\frac{\sigma_{vdW}}{r_{ij}}\right)^m\right],$$

parameterized to match the decay of the van der Waals energy $u_{vdW}^{analytical}(r)$ as a function of the center-to-center distance r for a pair of cubes with edge length $L_C = 87$ nm, oriented with two faces maximally aligned, calculated using analytical expressions derived elsewhere:[2,3]

$$u_{vdW}^{analytical}(r) = -\frac{H}{\pi^2} K(x)\Big|_{d+C_L, d+C_L}^{d+2C_L, d} \tag{S1}$$

where H is the Hamaker constant (2.30 eV) and

$$K(x) = \frac{1}{4}\ln\left(\frac{x^4 + 2x^2 L_C^2 + L_C^4}{x^4 + 2x^2 L_C^2}\right) + 2\left(\frac{x^2 - L_C^2}{4L_C x}\right)\tan^{-1}\left(\frac{L_C}{x}\right) + \frac{x(2L_C^2)^{3/2}}{6L_C^4}\tan^{-1}\left(\frac{x}{(2L_C^2)^{1/2}}\right)$$
$$+ 2L_C\left(\frac{1}{6x^2} + \frac{1}{6L_C^2}\right)(x^2 + L_C^2)^{1/2}\tan^{-1}\left(\frac{L_C}{(x^2 + L_C^2)^{1/2}}\right).$$

All simulations used the values $\sigma_{vdW} = 14.5$ nm, $\varepsilon_{vdW} = 0.177$ eV, $n = 9$, and $m = 4.2$, fitted to match the decay of the pairwise vdW attraction between AuNCs (Figure 1b). The total interaction potential for

pairs of AuNCs as a function of relative orientation is shown in Supplementary Fig. 2 for three different values of λ.

Molecular dynamics simulations. We ran all simulations in *HOOMD-Blue* version 3.7.[4,5] The CG model was implemented as a rigid body of the interaction sites described above. For simulations of self-assembly from disorder, systems were initialized with 400 particles on a hexagonal lattice with a lattice constant of 200 nm (well beyond nearest neighbor distances in the assembled states) with random orientations in a large simulation box (particle number density 3.26×10^{-6} nm^{-2}). For the SQ-to-RB reconfiguration simulation (Figure 5h,i), we used the configuration from the first experimental snapshot (Figure 5b, 0 s) as the initial configuration and simulated at $(Q, \lambda) = (350\ e^-, 10$ nm$)$; for the RB-to-SQ reconfiguration simulation (Figure 5j,k), we used the final snapshot of the assembly simulation at $(Q, \lambda) = (500\ e^-, 8$ nm$)$ (Figure 2d, $1.4 \times 10^8\ \delta t/\tau$) as the initial configuration and simulated at $(Q, \lambda) = (350\ e^-, 6$ nm$)$. System trajectories were generated using Brownian dynamics with a timestep $\delta t = 0.01\tau$ where τ is the natural time unit of the simulation. We used a translational drag coefficient of $0.5\ m_u\tau^{-1}$ and a rotational drag coefficient of $1.667\ \tau^{-1}$, where m_u is the mass of a single AuNC. To accelerate the formation of a single aggregate of particles as observed experimentally, we applied a small focusing force that pushes each particle towards the center of the simulation box. To apply the focusing force, we used a Gaussian potential of the form $u_{\text{foc}}(r_i) = C_{\text{foc}} \exp\left(-\frac{1}{2}\left(\frac{r_i}{\sigma_{\text{foc}}}\right)^2\right)$, with $C_{\text{foc}} = 1.0$ kT and $\sigma_{\text{foc}} = 1000$ nm. Simulations were run for a minimum of $1 \times 10^6\ \tau$, or until structural metrics stabilized for $2 \times 10^5\ \tau$. All simulations were performed on NVIDIA A100 GPUs on the NCSA Delta cluster, which is part of the NSF ACCESS resource. The computational workflow and data management for this publication was supported by the *signac* data management framework.[6,7]

General analysis of simulation data. We utilized the *freud* Python library for analysis of simulation data.[8] We calculated ψ_{mj} and ϕ_{4j} using the same nearest-neighbor criteria as for the experimental data (details in Supplementary Note 10).

Lattice offset order parameter. We developed and used a *lattice offset order parameter* O_L to quantify the local structure in the system, reported as

$$\langle O_L \rangle = \frac{1}{N_T} \sum_{i=1}^{N_T} \left(\frac{1}{N_i} \sum_{j=1}^{4} O_{L,ij} \right)$$

where N_T is the total number of particles in the system with at least 4 nearest-neighbors, N_i is the number of nearest-neighbors of particle i using the same nearest-neighbor criteria for ψ_{4j}, and $O_{L,ij}$ is the local lattice offset between particles i and j. We calculated $O_{L,ij}$ by creating the right triangle whose hypotenuse is $\vec{r}_{ij}$ and whose base is the vector that extends from the center of particle i and is perpendicular to the edge of particle i, as shown in Figure 1e. O_L is then the other leg of the right triangle, shown as the red line in Figure 1e.

Local lattice angles. We report the local lattice angles as the distribution of bond angles between particles in the system. The bond angles are the angles between consecutive nearest-neighbor vectors of a single particle. We used the same nearest-neighbor criteria as for ψ_{6j} with the exception that r_{cut} was set to $\sqrt{2}\langle r_{NN} \rangle$, where $\langle r_{NN} \rangle$ is the mean nearest neighbor distance in the system.

Supplementary Note 2. Robustness of self-assembly behavior to charge asymmetry

The charge density on the surface of a conducting object is a function of the local curvature, yet the exact distribution is nontrivial.[9] We tested the effect of charge distribution on AuNC self-assembly behavior with the CG model by running the assembly simulations at different values of the charge asymmetry factor f_{CA}. We observed the self-assembly of all three superlattice structures for each of the three values of f_{CA} we examined (1, 2, and 3). The scaling theory readily collapsed our simulation data into a separate master curve for each f_{CA} as shown in Supplementary Fig. 1. The key effect of an increasing f_{CA} was to increase the value of O_L for each (Q, λ) state point studied, indicating that increased charge asymmetry can slightly increase the deviation from perfect square packing; we also observed a slight difference in the fitting parameters of the scaling theory for each f_{CA}, shown in Supplementary Table 1. However, we did not see a qualitative difference in the phase diagram, as the same phase was observed at each (Q, λ) state point across all f_{CA} values simulated. This result indicates the general phase behavior is insensitive to the charge distribution on the AuNCs.

Supplementary Note 3. Scaling theory

We hypothesized that the balance between van der Waals (vdW) attraction and screened electrostatic repulsion between AuNCs drives the phase transitions between square-like, rhombic, and hexagonal rotator phases. In this hypothesis, the hexagonal rotator crystal appears when the balance between interparticle attraction and repulsion results in an average interparticle spacing that is large enough to allow particles to freely rotate. In contrast, when the solvent sufficiently screens the electrostatic repulsion, particles can align in a face-to-face arrangement to maximize vdW contacts between neighboring particles. In the intermediate regime, the electrostatic repulsion prevents direct face-to-face alignment, but the interparticle spacing prohibits free rotations of particles.

To test our hypothesis, we did a scaling analysis of the relevant physical quantities and derived a principle of corresponding states curve. In the analysis, we consider the following physical variables, with dimensions denoted as combinations of mass [M], length [L], and time [T]:

- H [ML^2/T^2]: The Hamaker constant of the particle interacting through the solvent medium; H dictates the size-independent strength of the vdW attraction.
- C_{rep} [ML^2/T^2]: The magnitude of the repulsive potential between cubes which we approximate as the prefactor to the screened repulsive potential between two cubes; $C_{rep} = \frac{Q^2}{4\pi\varepsilon_r\varepsilon_0}$ where ε_0 and ε_r are the permittivity of free space and of the 1:1 (v:v) octanol–butanol mixture (7.74),[1] respectively.
- $k_B T$ [ML^2/T^2]: The temperature T of the system multiplied by the Boltzmann constant k_B, which sets the thermal energy scale.
- O_L [L]: the lattice offset order parameter (*vide supra*).
- λ [L]: The screening length of the solvent.
- L_C [L]: Edge length of the nanocubes, which dictates the range and magnitude of the vdW attraction.

We have 6 variables and 3 physical quantities, necessitating 3 dimensionless quantities Π to describe the relationship between all 6 variables. Dimensional analysis yields

$$\Pi_1 = H^2/C_{rep}k_B T$$

$$\Pi_2 = O_L/\lambda$$

$$\Pi_3 = L_C/O_L.$$

From the Buckingham Pi theorem,

$$\Pi_3 = f(\Pi_1, \Pi_2).$$

We found that all of the data falls onto a master curve of the form

$$\Pi_3 = Z\Pi_1^\gamma \Pi_2^\zeta,$$

where Z, γ, and ζ are fitting parameters; we found optimal data collapse with $\gamma = -0.159$, $\zeta = 0.497$, and $Z = 2.185$ for the data presented in Figure 1f. Given the functional form of the master curve, we can express O_L as a function of the screening length and the total charge of each cube as

$$O_L = \left[Z\gamma \left(\frac{H^2}{C_{rep} k_B T} \right) L_C \right]^{\frac{1}{\zeta+1}}$$

Hence, this scaling theory allows us to predict the combinations of charge and screening length that give the same offset length as experiments.

Supplementary Note 4. Prediction of the rhombic-to-hexagonal rotator transition

The scaling theory described in Supplementary Note 3 enables the prediction of the lattice offset length for a given AuNC system but does not predict transitions between lattices with different symmetries. We can, however, locate the RB–HR transition using a combination of geometric and energetic considerations. In particular, we posit that the system forms a rotator phase when the center-to-center distance that minimizes the pairwise potential energy is greater than the circumsphere diameter of the AuNCs ($L_C\sqrt{2}$) plus the solvent screening length to account for the change in effective size of AuNCs in different solvent conditions, as the AuNCs can freely rotate without colliding with neighbors at this separation distance. The addition of λ estimates the increase in size of the effective shape of the AuNCs due to electrostatic repulsion. We found $\lambda(Q)$ pairs where the equilibrium pairwise separation $r_{min} = L_C\sqrt{2} + \lambda$ (Figure 1f, blue line) by considering the total pairwise interaction energy to be the sum of vdW attractions (evaluated with Equation S1) and screened electrostatic interactions. We evaluated the screened electrostatic repulsion as the electrostatic repulsion between two like-charged spherical shells of charge Q with radii R equal to the radius of the insphere of the AuNCs such that the surface-to-surface distances for the spheres and AuNCs are equal. The electrostatic repulsion is then given by

$$u_{el}^{analytical}(r_{ij}) = \frac{Q^2}{4\pi\varepsilon_r\varepsilon_0 \left(1 + \frac{R}{\lambda}\right)^2} \cdot \frac{e^{\frac{-(r_{ij} - 2R)}{\lambda}}}{r_{ij}}$$

Supplementary Note 5. Synthesis and ligand exchange of gold nanoparticles

Chemicals. Gold(III) chloride trihydrate (HAuCl$_4$·3H$_2$O, $\geqslant$99.9% trace metals basis), L-ascorbic acid (AA, $\geqslant$99.5%), silver nitrate (AgNO$_3$, $\geqslant$99.0%), sodium borohydride (NaBH$_4$, 99%), hydrochloric acid (HCl, 37 wt% in water), nitric acid (HNO$_3$, 70%), tetrahydrofuran (THF, ACS reagent, $\geqslant$99.0%) were purchased from Sigma Aldrich. Hexadecyltrimethylammonium bromide (CTAB, >98.0%), 1-butanol (BuOH, >99.0%) were purchased from TCI America. n-Octane (> 98%) was purchased from Alfa Aesar. Potassium bromide (KBr, 99.999 %) was purchased from Acros Organics. Thiol-terminated polystyrene (PS-SH, M_n = 3000, M_w = 3200) was purchased from Polymer Source, Inc. All chemicals were used as received without further purification. Ultrapure water (18.2 MΩ·cm at 25 °C) obtained from a Barnstead® GenPure® water

purification system (Thermo Scientific) was used in all experiments. All glassware were cleaned with aqua regia (a mixture of HCl and HNO_3 (v:v = 3:1)), rinsed thoroughly with water and dried before use.

Synthesis of gold nanocubes. Gold nanocubes were synthesized via iterative reductive growth and oxidative dissolution reactions based on a previously reported method with modifications.[10] Typical reactions include the following steps: (1) synthesis of gold nanorods (NRs), (2) iterative oxidative dissolution and reductive growth of NRs into spherical seeds, and (3) synthesis of nanocubes via seed-mediated growth.

(1) Synthesis of gold NRs. Gold NRs were prepared by using a seed-mediated growth method.[11] In a typical reaction, 125 μL of 10 mM $HAuCl_4$ was well-mixed with 5 mL of 100 mM CTAB in a 20 mL vial. Then, 300 μL of freshly prepared 10 mM $NaBH_4$ was rapidly injected into the mixture under vigorous stirring. The seed solution was aged at 30 °C for 1 h before use. The growth solution was prepared by successively mixing 800 mL of 100 mM CTAB, 40 mL of 10 mM $HAuCl_4$, 7.2 mL of 10 mM $AgNO_3$, and 4.56 mL of 100 mM L-ascorbic acid at 30 °C. Immediately after the addition of L-ascorbic acid, 960 μL of aged seed solution was added into the growth solution. The solution was gently stirred for 30 s and left undisturbed at 30 °C for 4 h. The products were isolated and purified via two cycles of centrifugation at $10950 \times g$ for 10 min, each time redispersed into 50 mM CTAB. The NR solution was finally adjusted to an optical density (O.D.) of 2.0 at the longitudinal plasmon peak wavelength using 50 mM CTAB (aq).

(2) Iterative oxidative dissolution and reductive growth of NRs into spherical seeds. Spherical gold seeds were synthesized through iterative reductive growth and oxidative dissolution of gold NRs. First, as-synthesized gold NRs were etched by adding an appropriate volume of 10 mM $HAuCl_4$ into the NR solution (O.D. = 2) to reach a final concentration of 75 μM of Au^{3+}. The solution was kept at 40 °C under stirring (ca. 200 rpm) for 4 h. The products were purified using two rounds of centrifugation at $11500 \times g$ for 20 min, each time followed by re-dispersion into 100 mM CPC (aq). Next, reductive growth of etched NRs into concave rhombic dodecahedra (CRD) and subsequent oxidative dissolution were conducted. To grow gold CRD, typically, 10 mL of 10 mM CPC, 175 μL of 10 mM $HAuCl_4$, and 2.25 mL of 100 mM L-ascorbic acid were mixed in succession. 3 mL of the etched NR solution (O.D. = 1.0) was then introduced to the mixture. The solution was gently stirred for 30 s and left undisturbed at 40 °C for 15 min. The CRD were isolated and purified by two rounds of centrifugation at $10950 \times g$ for 10 min, each time followed by redispersion into 50 mM CTAB (aq). Subsequent etching of the CRD (O.D. = 1.0) were induced by adding an appropriate volume of 10 mM $HAuCl_4$ to reach a final concentration of 60 μM of Au^{3+}. The reaction solution was kept at 40 °C for 4 h under stirring and the resultant spherical seeds were isolated and purified by two cycles of centrifugation at $11500 \times g$ for 10 minutes. The spherical seeds were finally dispersed in 100 mM CPC (aq) to reach O.D. = 1 at 524 nm.

(3) Synthesis of gold nanocubes. Typically, 0.4 mL of spherical seed solution (O.D. = 1.0 at 524 nm) was introduced to a mixture of 10 mL of 100 mM CPC, 1 mL of 100 mM KBr, 0.6 mL of 10 mM $HAuCl_4$, and 0.9 mL of 100 mM L-ascorbic acid. The solution was gently stirred for 30 s and left undisturbed at 30 °C for 1 h. The resultant gold nanocubes were purified by two rounds of centrifugation at $1540 \times g$ for 3 min, each time followed by redispersion into 50 mM CTAB (aq). Gold nanocubes were finally dispersed into 2 mL of 50 mM CTAB (aq) for further use.

Grafting PS-SH onto gold nanoparticles. Surface modification of gold nanocubes with PS-SH was conducted according to previously reported methods with modifications.[12-14] Typically, 0.5 mL of the pristine gold nanocube solution was first concentrated to ~100 μL via centrifugation at $1540 \times g$ for 3 min. Next, this concentrated gold nanocube solution was added dropwise into a 10 mL THF solution of PS-SH (2 mg·mL^{-1}) under sonication. The resultant mixture was left undisturbed for 24 h at room temperature.

Afterward, the PS-grafted gold nanocubes were purified using three rounds of centrifugation at $2740 \times g$ for 3 min, each time followed by re-dispersion into 3 mL of THF. After the last centrifugation step, the PS-grafted gold nanocubes were dispersed in 200 μL of THF for LCTEM experiments.

Supplementary Note 6. Effect of polymer–polymer and polymer–solvent interactions on self-assembly

Here, we present an analysis that shows that changes in polymer–polymer and polymer–solvent interactions with changing solvent cannot explain the observed changes in self-assembly behavior in this study. Interactions between polymer brushes on nearby particles are negligible if the brushes are separated by more than the characteristic decay length of solvophobic interactions, which is ~1 nm.[15,16] Considering two nanocubes with the closest surface-to-surface distance D, each coated by a polymer brush of thickness h, the interparticle polymer–polymer surface distance is $D - 2h$ and polymer–polymer and polymer–solvent interactions are negligible when $D - 2h \gtrsim 1$ nm. Analysis of the LCTEM imaging presented in the main text shows that D is always greater than 15 nm during the assembly process (and only drops below 15 nm in the most polar solvent *after assembly has occurred* when the superlattice begins to contract, Supplementary Fig. 21). Hence, the most conservative condition allowing the neglect of these interactions is $h < 7$ nm, and we proceed by estimating h.

The condition to neglect polymer–polymer interactions relies on the thickness of the polymer brush height, h. To estimate h, we first establish that each solvent is a poor solvent for polystyrene. We then measure h by measuring the interparticle surface-to-surface distance in the dry state where the polymer brush thickness is approximately the same as in poor solvent.[17]

The solvents used in the work are as follows: 0:1, 1:1, and 4:1 v/v octane/butanol. We computed the polymer–solvent interaction parameter χ_{ps} for each solvent using the Hildebrand solubility parameters:

$$\chi_{ps} = 0.34 + \frac{V_s}{RT}(\delta_p - \delta_s)^2,$$

where V_s is the molar volume of the solvent (163.5 and 91.5 cm^3/mol for octane and butanol, respectively), δ_p and δ_s are the Hildebrand solubility parameters of the polymer and solvent, respectively, R is the ideal gas constant (8.314 J/mol-K), and T is the temperature (298 K). We used $\delta_p = \delta_{\text{styrene}} = 19.0$ (MPa)$^{1/2}$ and $\delta_s = 23.1$, 15.6 (MPa)$^{1/2}$ for butanol and octane, respectively.[18] Following the approach of Ianiro et al.,[19] which neglects the solvent–solvent interaction term, we computed χ for two-component solvent mixtures χ_{mix} as the volume-averaged solubility parameter for the polymer in each of the pure solvents:

$$\chi_{\text{mix}} = \phi_1\chi_1 + (1 - \phi_1)\chi_2,$$

where ϕ_1 is the volume fraction of the solvent with $\chi_{ps} = \chi_1$. $\chi_{ps} \geq 0.96$ for all solvents used in this work ($\chi_{ps} = 0.96, 1.03, 1.07$ for polystyrene in 0:1, 1:1, and 4:1 v/v octane/butanol, respectively, indicating that they are all poor solvents for polystyrene. We confirmed this conclusion by dispersing polystyrene in each solvent and in THF (to serve as a control) at 1 and 4 mg/mL. We observed rapid dissolution of polystyrene in THF, whereas the polymer remained insoluble in the three solvents used in this work (Supplementary Fig. 22a–b).

We further examined how this insolubility affects the dispersibility of the AuNCs in each solvent. After dispersing AuNCs in THF in Eppendorf tubes and drying under N_2, we added different solvents into each Eppendorf tube. After sonication, the AuNC residue remained on the walls of the tubes containing the

organic solvents used in this work, while the AuNCs formed a stable dispersion in THF (Supplementary Fig. 22c). These results are consistent with each solvent being a poor solvent for polystyrene.

Having established that polystyrene is insoluble in each of the three solvents used in this work, we can estimate h by first noting that the polymer thickness in poor solvent is approximately equal to that in a dry state. Santos et al. showed that the superlattice spacing of polystyrene-coated Au nanospheres differs by ~2% in poor solvent compared to the dry state.[17] We therefore estimated h as half of the mean interparticle surface-to-surface distance of AuNCs in the dry state, D_{dry}. Analysis of TEM images of dried AuNCs revealed $D_{dry} = 3.2 \pm 1.0$ nm so that $h = 1.6 \pm 0.5$ nm (Supplementary Fig. 23).

This value of h, combined with the observed interparticle surface-to-surface distance during self-assembly under LCTEM illumination, means that the polymer brushes on adjacent particles do not interact. As a result, these interactions cannot be responsible for any observed changes in assembly behavior in different solvents. Instead, longer-ranged interactions, such as van der Waals and electrostatics, must drive the observed behavior.

Supplementary Note 7. Effect of ligand shell repulsion on scaling theory

In Supplementary Note 6, we established that polymer–polymer and polymer–solvent interactions cannot drive the changes in assembly behavior with solvent that we observed. That analysis was based on the fact the polymer layers on neighboring AuNCs were too far apart to interact based on our measurements of the thickness of the polymer layers and the distributions of interparticle surface-to-surface distances during assembly. Here, we use a scaling argument to show that since all solvents are poor solvents for polystyrene, and therefore the properties of the polymer brush on the AuNC surface do not change with the solvent, any interactions involving the polymer ligands cannot explain the observed assembly behavior.

For polymer-coated cubes that are oriented face-to-face, the Alexander–de Gennes equation describes the polymer-induced repulsion U_{brush} as they are brought into contact[16,20]:

$$U_{brush}(D) = \begin{cases} \dfrac{L_c^2 h k_B T}{s^3}\left[\left(\dfrac{2h}{D}\right)^{\frac{9}{4}} - \left(\dfrac{D}{2h}\right)^{\frac{3}{4}}\right] & D < 2h \\ \\ 0 & D \geq 2h \end{cases}$$

where D is the distance between the surfaces, L_c is the edge length of the AuNCs, h is the thickness of the polymer brush, k_B is Boltzmann's constant, T is temperature, and s is the average distance between polymer attachment points on the surface. Rederiving the scaling theory to include quantities that influence the short-ranged brush repulsion and neglect the quantities related to the longer-ranged electrostatic repulsion (i.e., replace C_{rep} and λ with h and s), we again obtain 3 dimensionless quantities $\Pi_{i,brush}$ from 6 variables ($H, h, L_C, O_L, k_B T, s$):

$$\Pi_{1,brush} = HhL_C/k_B T O_L^2$$

$$\Pi_{2,brush} = HhL_C/k_B T s^2$$

$$\Pi_{3,brush} = hL_C/O_L s$$

Note that if the brush properties h and s do not change in these equations, all the dimensionless quantities remain constant. Since all three solvents chosen in this work are poor solvents with χ parameters that are approximately equal (the calculated χ parameters vary by a few percent, see Supplementary Note 6), h and

s should remain constant across all systems that we studied. Our new dimensionless quantities therefore remain constant when changing the solvent, indicating that brush repulsion cannot drive a change in O_L.

Supplementary Note 8. In-situ LCTEM imaging

In-situ LCTEM imaging. In-situ LCTEM imaging was performed on a JEOL JEM 1400plus microscope using a Protochips Poseidon Select holder. Bottom E-chips with a 150 nm integrated gold spacer (EPB-52DF-10) and top E-chips with the nominal window dimension of 550 μm × 20 μm (EPT-52W-10) were used in all experiments. LCTEM movies were recorded with a Gatan OneView CMOS camera capable of recording 4k × 4k images at a frame rate of 5 fps.

In a typical experiment, the three polyether ether ketone (PEEK) internal capillary tubings of the Poseidon holder were flushed with the solvents to be used for LCTEM imaging for 10 min each to remove trapped air and to prime the lines before loading of the E-chips. Excess liquid exiting the holder tip was wicked away with a Kimwipe. Separately, E-chips were soaked in acetone followed by methanol for 2 min respectively to remove the photoresist protective coatings. After blow drying with nitrogen, the E-chips were further plasma cleaned for 2 min (Harrick PDC-001 expanded plasma cleaner). Next, one bottom E-chip was placed into holder tip and seated properly, and 1 μL of gold nanocube solution in THF was added. After the solvent was dried, a small drop of the solvent to be used for LCTEM imaging was drop-casted onto the bottom E-chip, and the large E-chip was positioned on top to form a sandwich. After securing the metal lid with three brass screws, solvent was flowed for 10 min using a syringe pump (flow rate: 5 μL /min) to remove trapped air bubbles within the microfluidic channel. After performing a leak check with a dry pumping station, the Poseidon holder was inserted into the JEOL JEM 1400plus microscope and was used in a quiescent state to minimize the influence of solvent flow on particle motion behaviors. The liquid layer thickness near the center of the cell can exceed 1 μm due to the bulging of the Si_3N_4 windows under vacuum. Therefore, movies were typically acquired near the corner regions of the liquid cell. We found that the use of low-vapor-pressure solvents such as octane and butanol was crucial for long-duration LCTEM imaging. By contrast, rupturing of the Si_3N_4 window usually occurred within 5 minutes of electron beam illumination when more volatile solvents such as THF were used. An electron dose rate of 14.0 e⁻·Å⁻²·s⁻¹ was used for LCTEM imaging, which is much lower than that often employed for studying nanoparticle growth or dissolution.[21-26] For the rapid solvent-exchange experiments shown in Figure 5, we used a higher flow rate (20 μL/min) to flow in the new solvent. Experimentally, we found that the delay between starting the syringe pump and arrival of the new solvent in the field-of-view is ~43 s.

LCTEM electron dose rates. Electron dose rates (unit: e⁻·Å⁻²·s⁻¹) were calculated based on the TEM image intensity under identical imaging conditions except for the absence of any specimen in the electron beam path.

$$\text{Electron dose rate} = \frac{I}{74.7At},$$

where 74.7 is the conversion factor between pixel intensity and number of electrons for our OneView CMOS camera obtained with a Faraday cup holder at 120 kV. I is the total pixel intensity of a TEM image, A is the image area and t is exposure time.

Supplementary Note 9. Image segmentation of LCTEM movies based on deep learning algorithm

The flowchart in Supplementary Fig. 5 summarizes the key steps of image processing and analysis. Variations in nanocrystal brightness/contrast and fluctuating background intensity that are often associated

with LCTEM movies render the conventional threshold-based image segmentation method unsatisfactory. To overcome this challenge, we employed a U-Net-based model for the segmentation of LCTEM movie frames and particle identification (Supplementary Fig. 6). U-Net is a deep convolutional neural network characterized by a U-shaped architecture consisting of a contracting path to capture the context of the input image and a symmetric expansive path that enables precise localization.[27]

Typically, three LCTEM images selected from distinct stages of the assembly process were manually labelled using ImageJ to obtain their corresponding binarized images. The three image pairs were augmented using the Python library *Albumentations* to generate a large training dataset consisting of 600 image pairs.[28] Augmentation operations include image rotation, changing brightness, and vertical and horizontal flipping. The new dataset was used to train the U-Net model, which allowed for high-accuracy identification of particle contours and centroids for the entire LCTEM movie (Supplementary Fig. 6).

Supplementary Note 10. LCTEM image processing and quantitative analysis of density and symmetry of nanocube superlattices

Image processing. As detailed in Supplementary Note 9, raw LCTEM movie frames were processed using a U-Net-based model to obtain segmented images. Afterward, fast Fourier transform patterns of the images were created. Next, the contours and centroids of individual nanocubes were determined using custom-written MATLAB scripts. The nanocube orientation and coordinates of nanocube centroids were used for quantitative analyses of symmetry and density of nanoparticle assemblies.

Radial distribution function. The spatial distribution of nanoparticles was quantified by calculating the radial distribution function $g(r)$ using a custom-written MATLAB script. $g(r)$ indicates the probability of finding another particle at a given distance r from the reference particle and is defined as[29]

$$g(r) = \frac{\rho(r)}{\rho_0},$$

where $\rho(r)$ is the particle number density at the distance r and ρ_0 is the average particle number density. The spatial decay and peak linewidth of $g(r)$ reveal the degree of translational order.

Nanocube orientation. The nanocube orientation (θ) was defined as the angle between one edge of the nanocube and a reference axis, which we took to be the positive x-axis. By symmetry, $0° \leq \theta < 90°$.

Bond-orientational order parameter. The m-fold bond-orientational order parameter of each particle j (ψ_{mj}) was used to quantify the local hexagonal ($m = 6$) or tetragonal ($m = 4$) order of nanocube assemblies. For a 2D colloidal system, ψ_{mj} is given by[30-33]

$$\psi_{mj} = \frac{1}{N} \sum_{k=1}^{N} \exp(im\theta_{jk}),$$

where i is the imaginary unit, θ_{jk} is the angle between the bond connecting particle j and its nearest neighbor particle k and an arbitrary reference axis, and N is the total number of nearest neighbors for particle j. With this definition, any particle whose bonds have perfect hexagonal order has $|\psi_{6j}| = 1$, even if N < 6. We assigned $|\psi_{6j}| = 0$ for particles with N $\leq$ 2, and $|\psi_{4j}| = 0$ for particles with N $\leq$ 1, similar to previous work.[34] By contrast, particles with random bond angles have low $|\psi_{mj}|$. We considered two particles j and k to be nearest neighbors if they meet the following two criteria: their Voronoi cells share an edge (or, equivalently, the particles are connected in the Delaunay triangulation of the system)[35] and their

interparticle distance $|\vec{r}_{ij}| < r_{cut}$,[35,36] where we used the location of the first minimum after the first peak of $g(r)$ as r_{cut} for ψ_{6j} and 1.2 times the location of the first peak of $g(r)$ for ψ_{4j}.[36,37] Additionally for ψ_{4j}, we limited $N \leq 4$ by only considering up to 4 nearest neighbors of each particle.[35] Bond networks connecting nearest neighbors are shown in Figs 2a, 3a, 4a, and 5a and Supplementary Movies 4, 6, 7, 10, 13.

Particle orientational order parameter. The 4-fold particle orientational order parameter (ϕ_{4j}) was used to quantify the local orientational order of nanocube assemblies. For a 2D colloidal system, ϕ_{4j} is given by[37,38]

$$\phi_{4j} = \frac{1}{N+1}\left[\exp(i4\theta_j) + \sum_{k=1}^{N} \exp(i4\theta_k)\right],$$
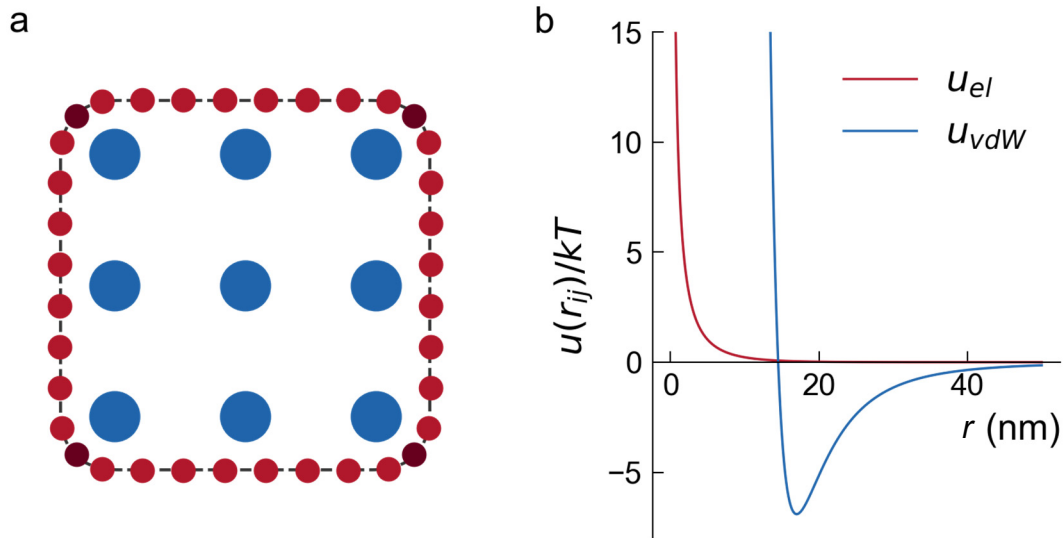
where θ_j (θ_k) is the angle of orientation defined above for nanocube j (its nearest-neighbors k) and N is the number of nearest neighbors of nanocube j. For a given movie, the criteria for determining nearest neighbors when calculating ϕ_{4j} are the same as those for calculating either ψ_{6j} or ψ_{4j}. For movies where both ψ_{6j} and ψ_{4j} were analyzed, the nearest neighbor criteria when calculating ϕ_{4j} follow those of ψ_{6j} calculation. $|\phi_{4j}| = 0$ indicates random orientations whereas $|\phi_{4j}| = 1$ indicates the same orientation between the reference particle and its neighbors.

Supplementary Tables
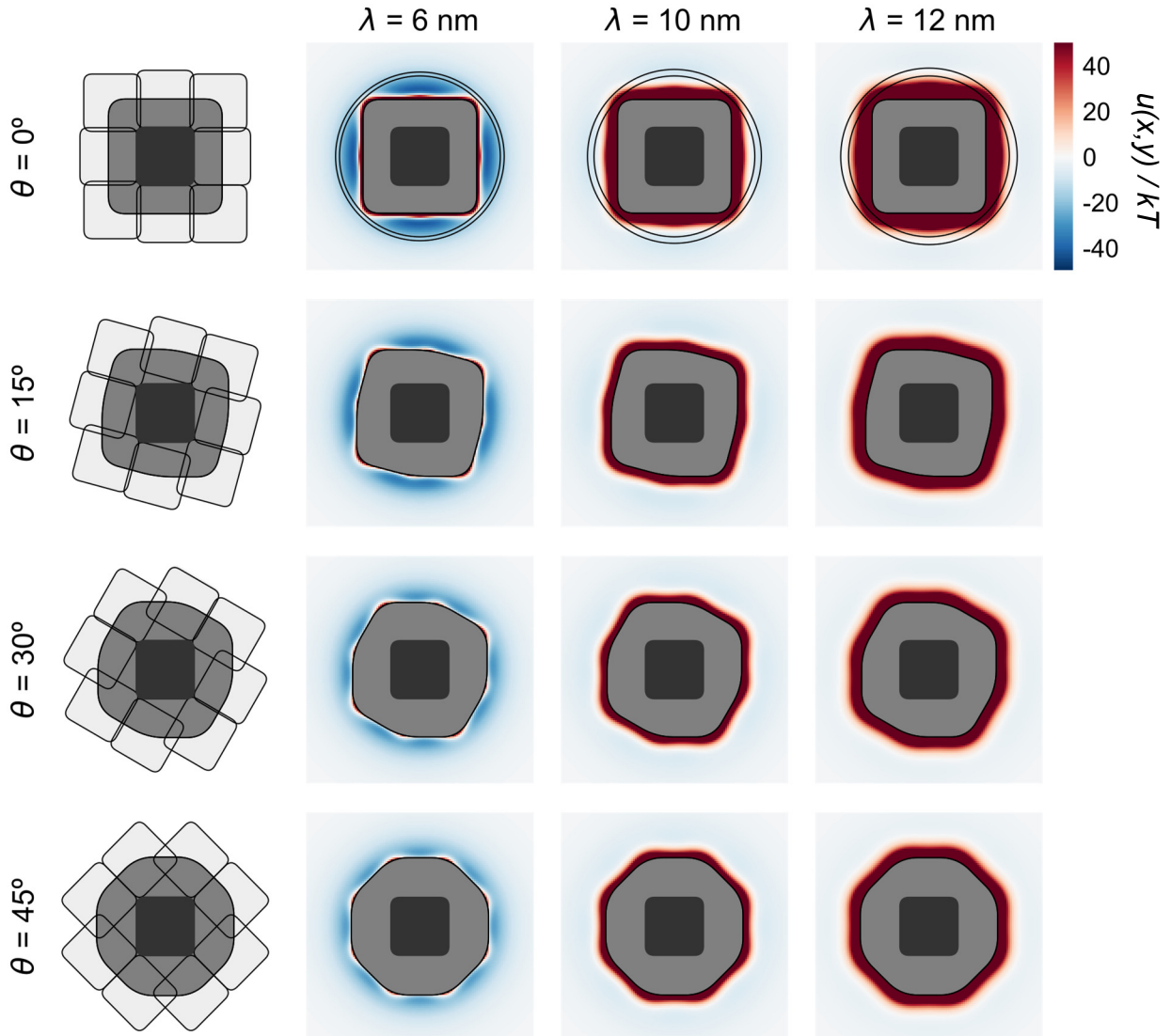
Supplementary Table 1: Fit for the scaling theory for different charge factors.

f_{CA}	Z	γ	ζ
1	2.267	-0.147	0.311
2	2.187	-0.158	0.435
3	2.185	-0.159	0.497
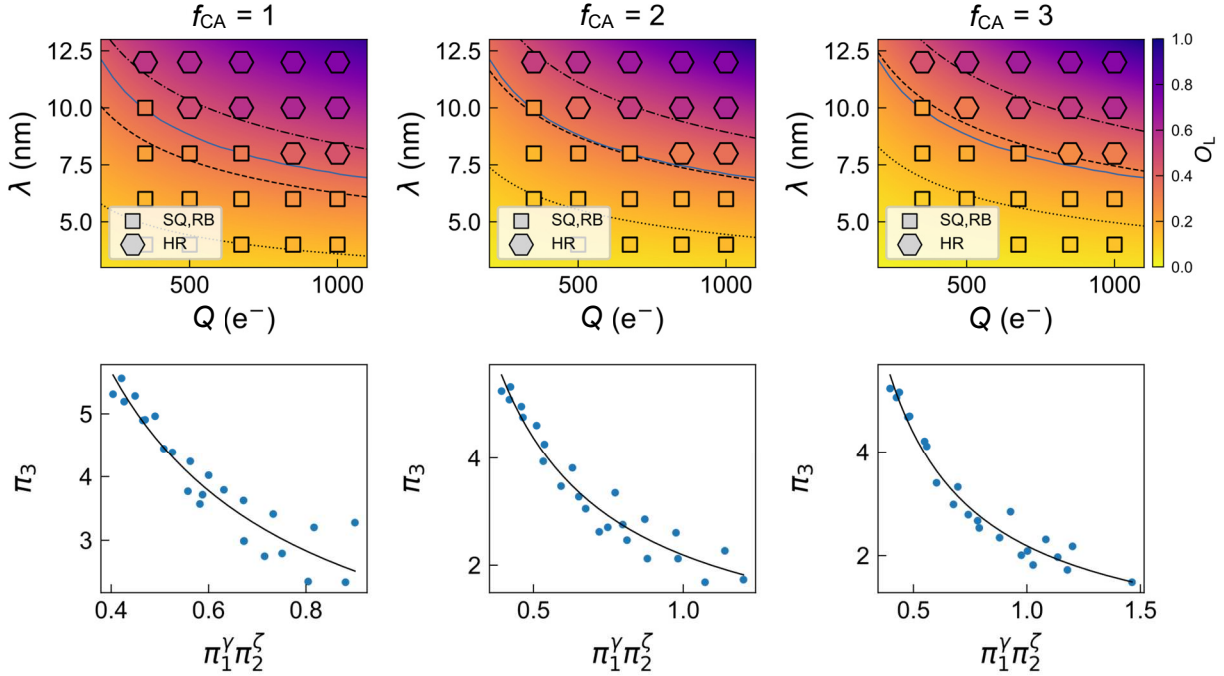
Supplementary Figures

a

b
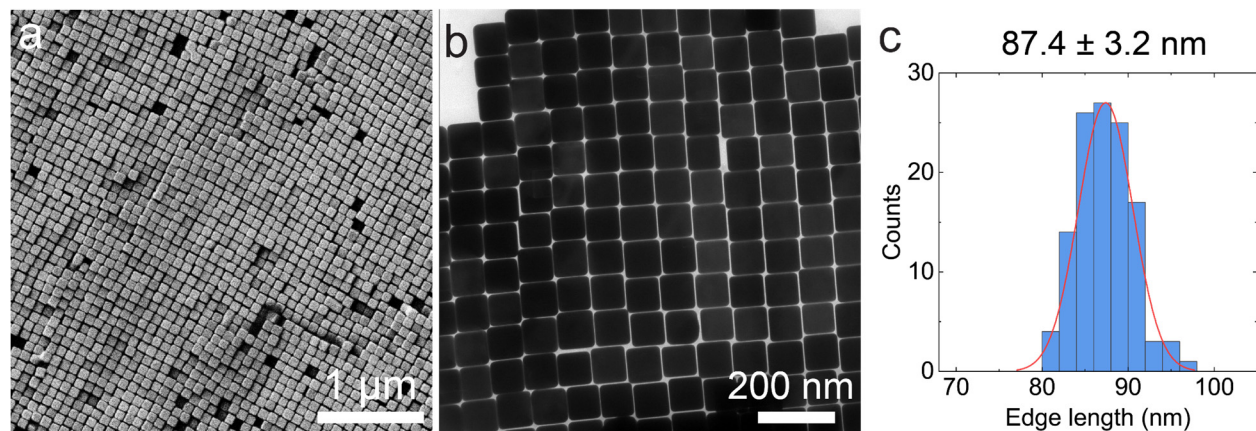
Supplementary Figure 1. Details of AuNC model used in molecular dynamics simulations. (a) Configuration of interaction sites within the AuNC particle model. Red sites represent the electrostatic interaction sites $\{s_{el}\}$ that interact with electrostatic interaction sites on neighboring AuNCs through the Yukawa potential shown in red in (b). The darker red sites are the corner sites that have a higher charge when $f_{CA} > 1$ (see Supplementary Note 1). Blue sites represent the van der Waals sites $\{s_{vdW}\}$ that interact through the Mie potential shown in blue in (b). The locations of the sites are drawn to scale, but the size of each site does not correspond to any parameters in the pair potentials. (b) Pair potentials through which sites on neighboring particles interact. All electrostatic (vdW) sites on one particle interact with all electrostatic (vdW) sites on neighboring particles, and electrostatic sites do not interact with any vdW sites. Note that charged sites are arranged so that they are on the surface of the AuNC, as depicted by the dashed line in (a).
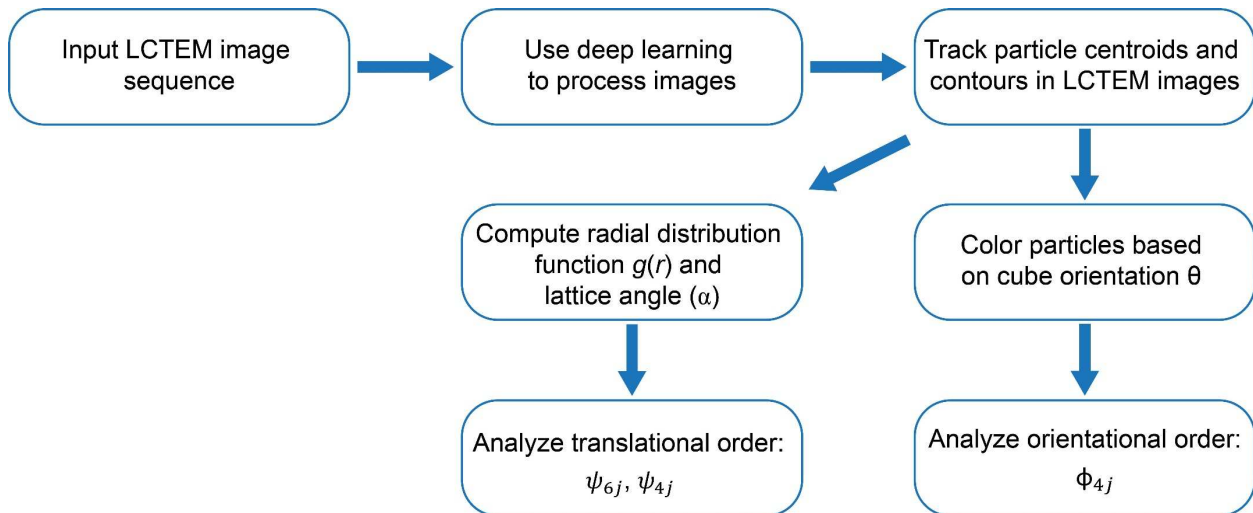
Supplementary Figure 2. Pair potential between AuNCs used in molecular dynamics simulations. The dark gray square in the center of each plot represents the position and orientation of the reference particle. The light gray region corresponds to the excluded volume region around the reference particle when considering volume exclusion interactions between the 87 nm edge length AuNC cores with a radius of curvature of $1/13$ nm^{-1} at the vertices. The leftmost column shows several positions of the test particle with fixed orientation θ as it sweeps around the perimeter of the reference particle while maintaining tangential contact. The next 3 columns show the pair potential between AuNCs with $Q = 350\ e^{-}$ at values of the screening length λ. All plots use the same color scale, shown to the right of the top row. The circles on the pair potential plots in the top row denote the circumcircle diameter and the circumcircle diameter plus the screening length (see Supplementary Note 4).
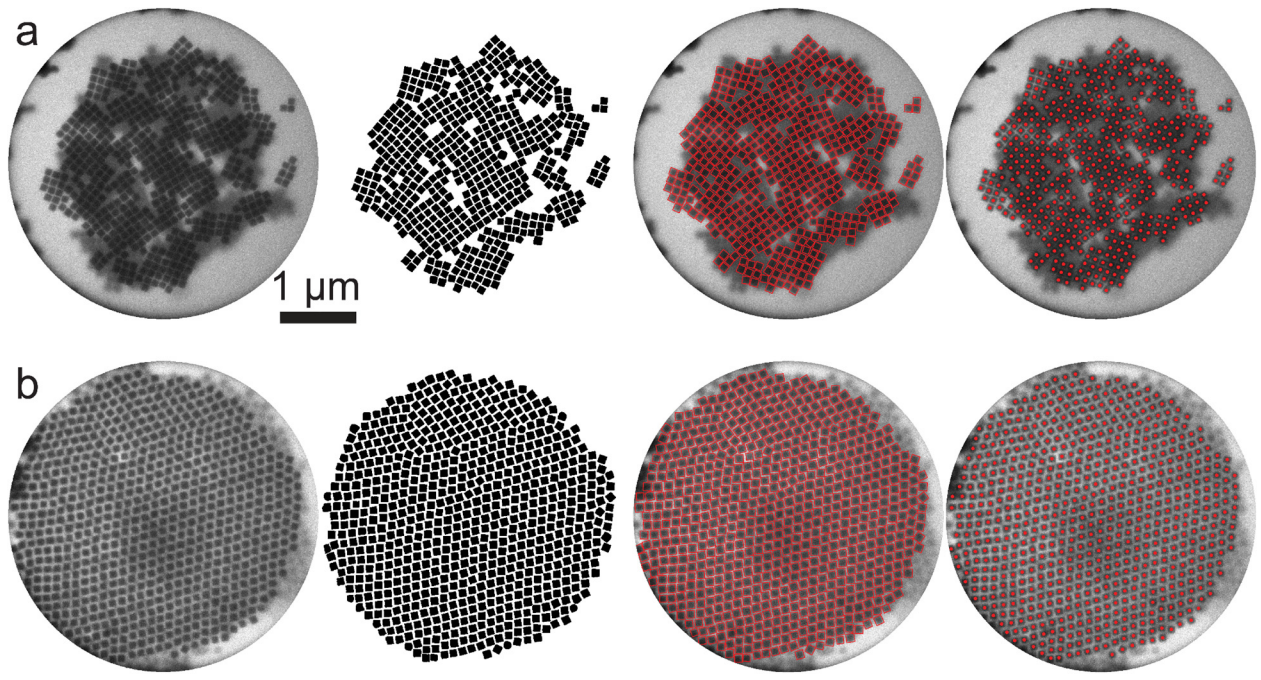
Supplementary Figure 3. Simulation phase diagram and scaling analysis for different charge asymmetry factors. (Top row) Phase diagrams for different values of f_{CA}. The color of the markers indicates the value of O_L observed in simulations at that point in the $Q\lambda$ plane. The background color indicates the value calculated from the scaling theory. The black lines are the offset values for the SQ (dotted), RB (dashed), and HR (dot-dashed) phases observed in LCTEM, and the solid blue line indicates the predicted stability limit of the HR phase (Supplementary Note 4). (Bottom row) Data collapse for different values of f_{CA}. The blue dots are the simulation values, and the black line is the curve fit to the power law form of the master curve (Supplementary Note 3).

17
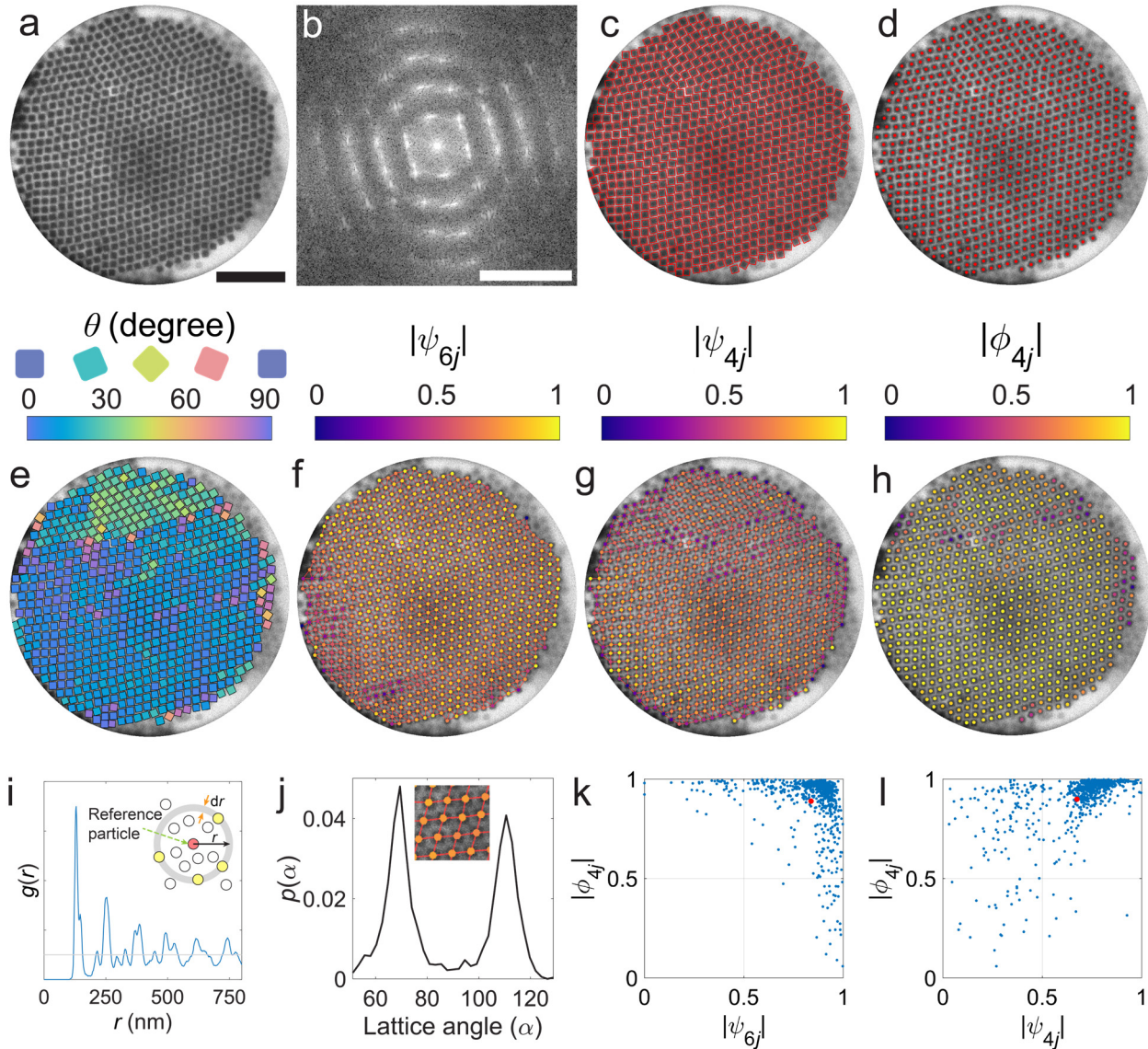
Supplementary Figure 4. Electron microscopy characterization of gold nanocubes. Representative (a) SEM and (b) TEM images of gold nanocubes and (c) nanocube edge length distribution histogram (average edge length: 87.4 ± 3.2 nm). The red curve represents a Gaussian fit to the histogram.
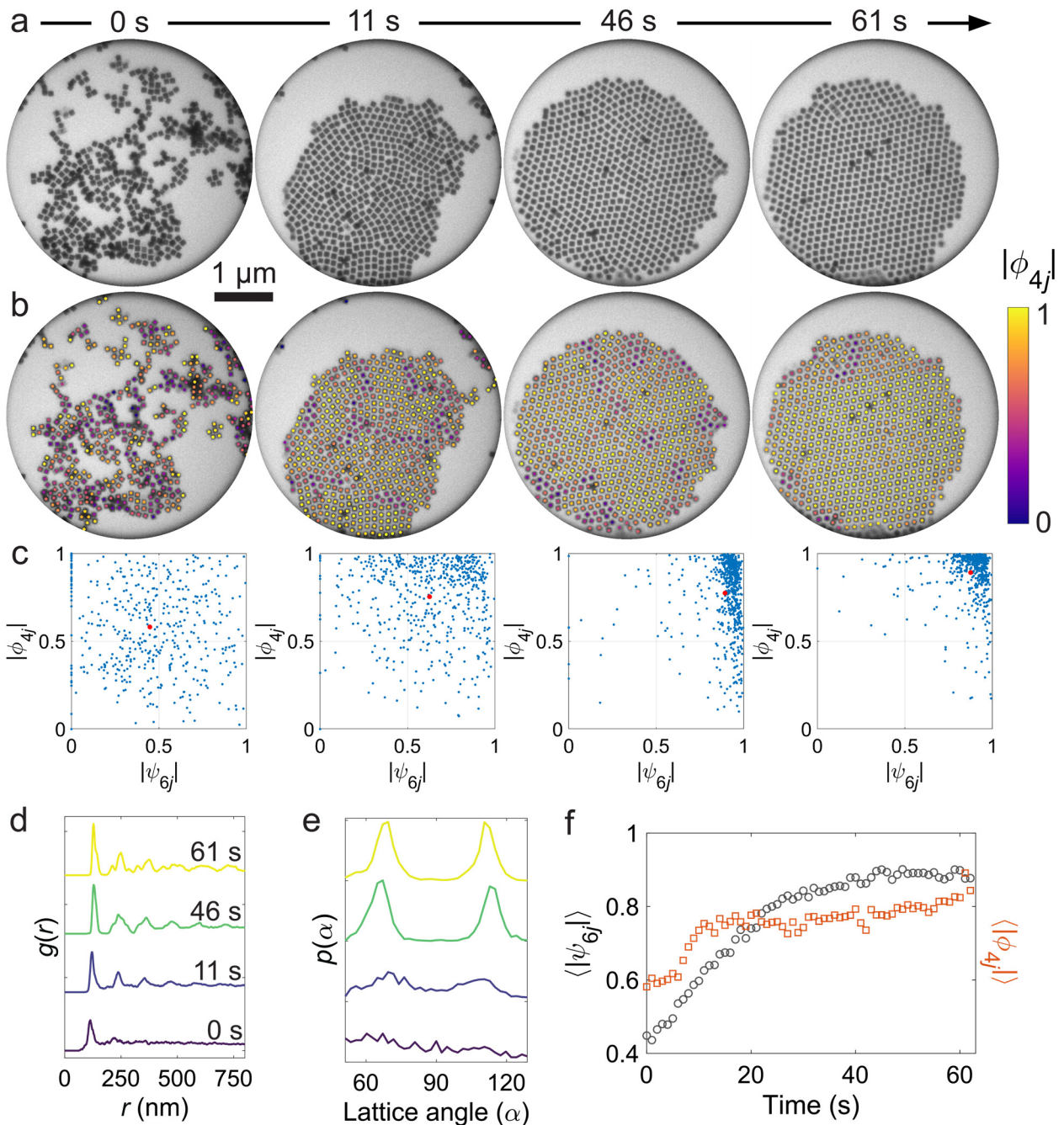
Supplementary Figure 5. A flowchart illustrating the general procedure of image processing and data analysis.
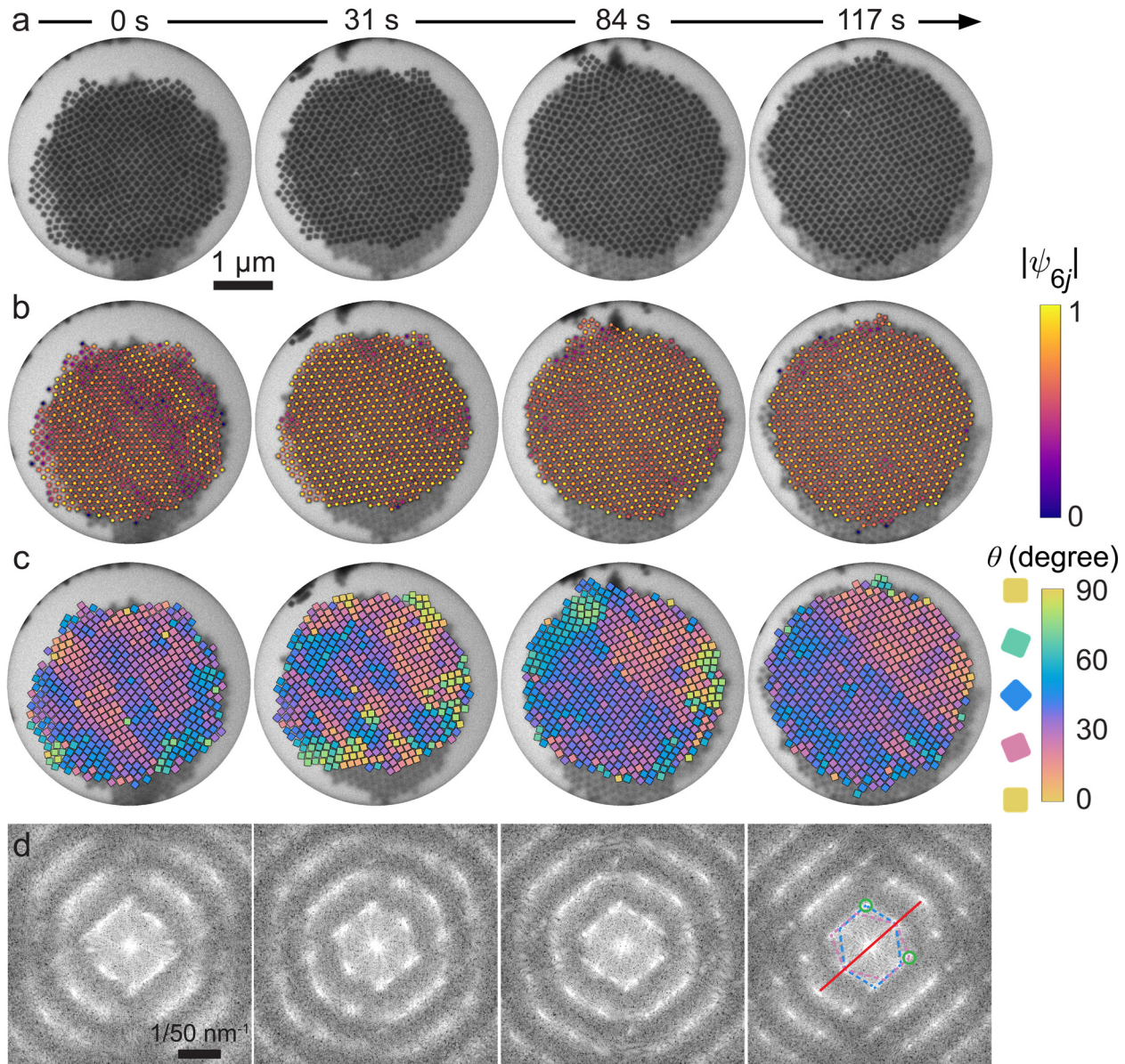
Supplementary Figure 6. Exemplary LCTEM images of gold nanocube superlattices showing satisfactory particle identification at different stages of the self-assembly process. From left to right: raw LCTEM movie frames, segmented images output by the U-Net model, raw LCTEM movie frames with particle contours and centroids overlaid for the (a) polycrystalline square-like and (b) the rhombic lattices.
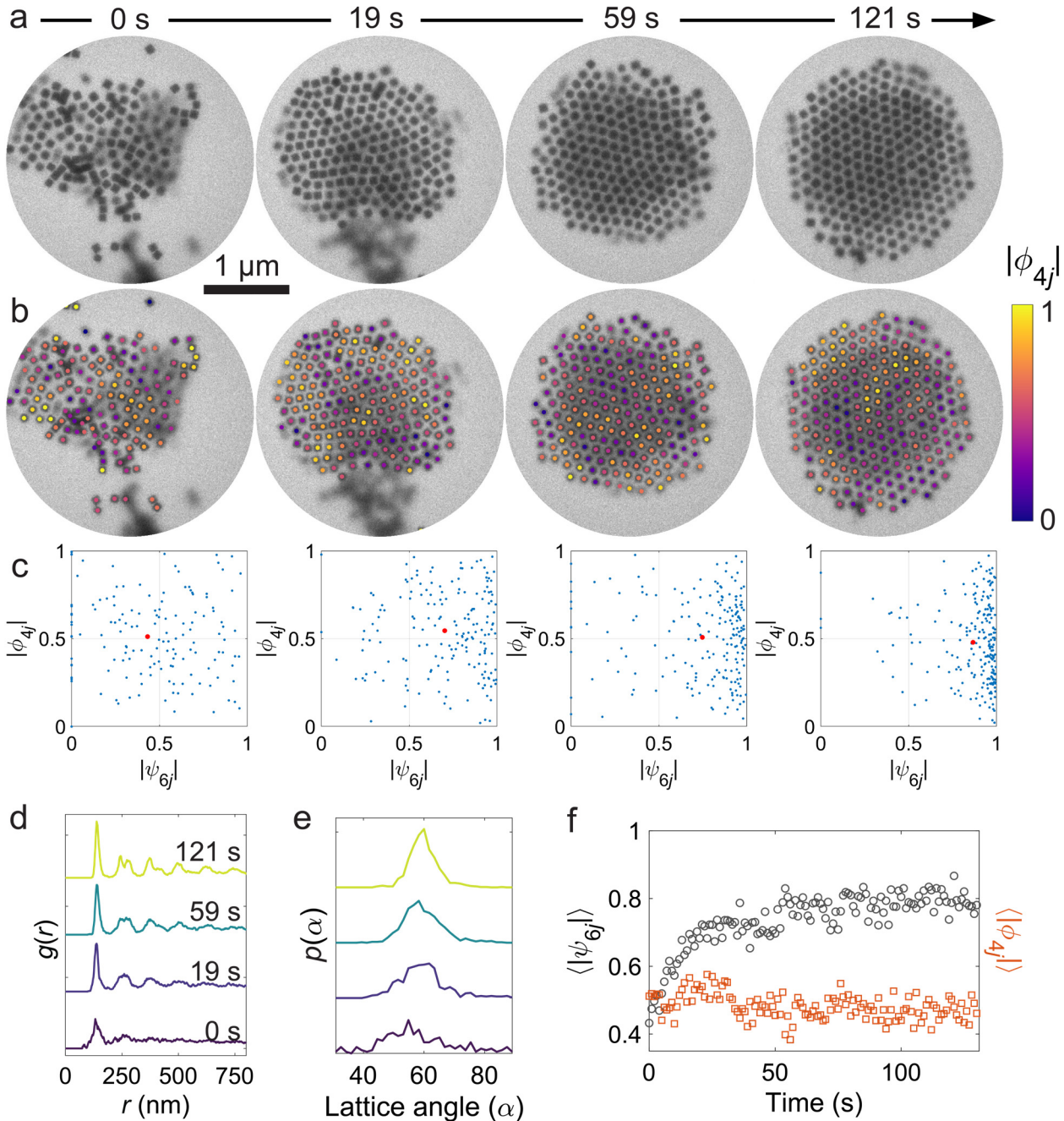
Supplementary Figure 7. Exemplary illustration of quantifying the translational and orientational order of the rhombic lattice. (a) LCTEM image, (b) corresponding FFT pattern, (c-d) identification of nanocube contours (c) and centroids (d). (e-j) The same LCTEM image with particles colored according to (e) nanocube orientation, (f) modulus of 6-fold bond-orientational order parameter $|\psi_{6j}|$, (g) modulus of 4-fold bond-orientational order parameter $|\psi_{4j}|$, and (h) modulus of 4-fold particle orientational order parameter $|\phi_{4j}|$. The nearest neighbors in (f) and (g) are connected by lines. (i) Radial distribution function $g(r)$ computed based on particle positions shown in (d). (j) Plots of lattice angle distribution corresponding to the LCTEM images. The inlet shows the rhombic superlattice bond network and corresponding two lattice angles. (k) 2D scatter plot of order parameters $|\psi_{6j}|$ and $|\phi_{4j}|$ for the LCTEM image shown in (a). (l) 2D scatter plot of order parameters $|\psi_{4j}|$ and $|\phi_{4j}|$ for the LCTEM image shown in (a). The red dots in (k) and (l) denote the mean values of the order parameters. Scale bars: (a) 1 μm, (b) 1/20 nm^{-1}.

21
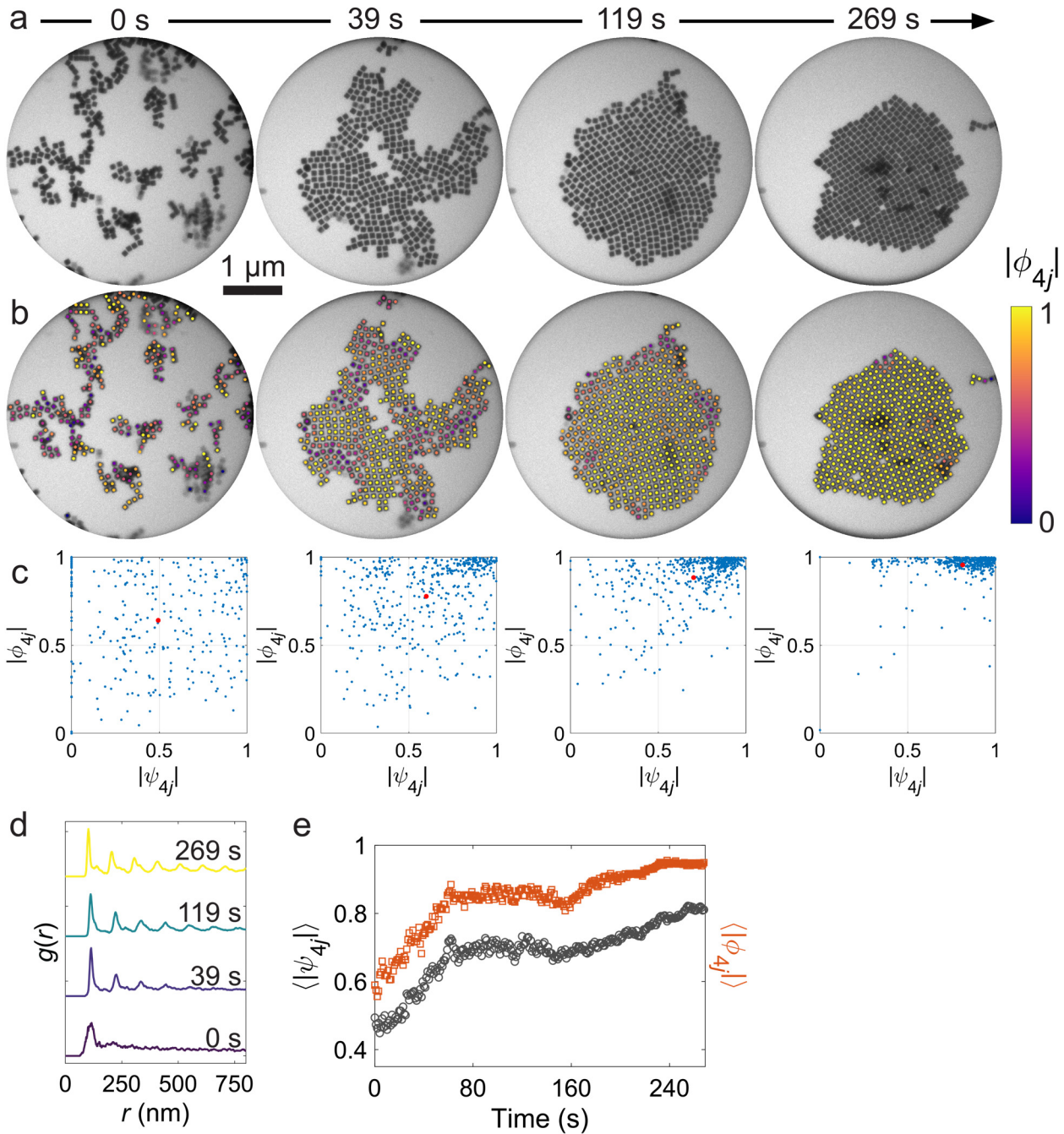
Supplementary Figure 8. **Quantitative analysis of translational and orientational order of the rhombic phase**. (a) Raw LCTEM images and (b) the same images overlaid with particle centroids colored according to $|\phi_{4j}|$. (c) 2D scatter plots of order parameters $|\psi_{6j}|$ and $|\phi_{4j}|$ for the four different stages shown in (a) and (b). The red dots denote the mean values of $|\psi_{6j}|$ and $|\phi_{4j}|$. (d-e) Plots of $g(r)$ (d) and lattice angle distribution $p(\alpha)$ (e) at selected time points. (f) Plots of ensemble-averaged $|\psi_{6j}|$ and $|\phi_{4j}|$ versus time.
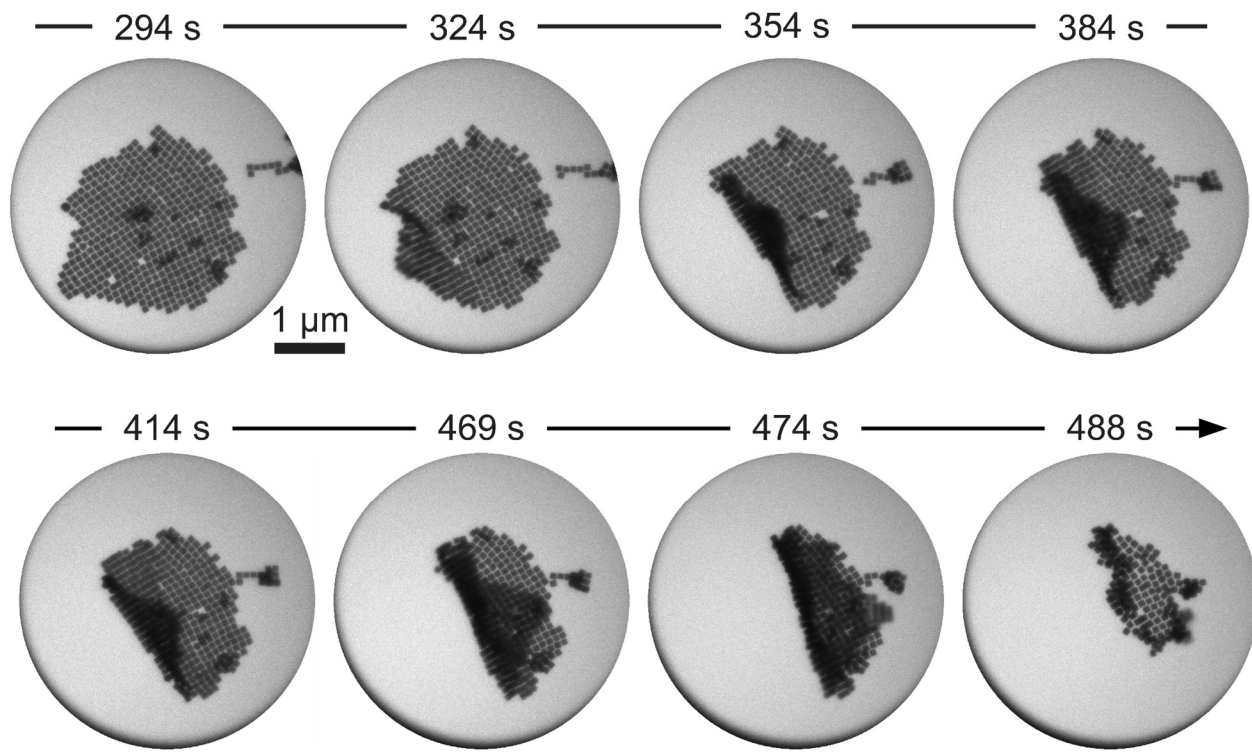
Supplementary Figure 9. **Formation of twin boundaries in the rhombic lattice**. (a) Raw LCTEM images, (b) the same images overlaid with particle centroids colored according to $|\psi_{6j}|$, and (c) nanocubes colored according to their orientations. (d) Corresponding FFT patterns. Two sets of FFT patterns from the twinned domains at 117 s are highlighted.
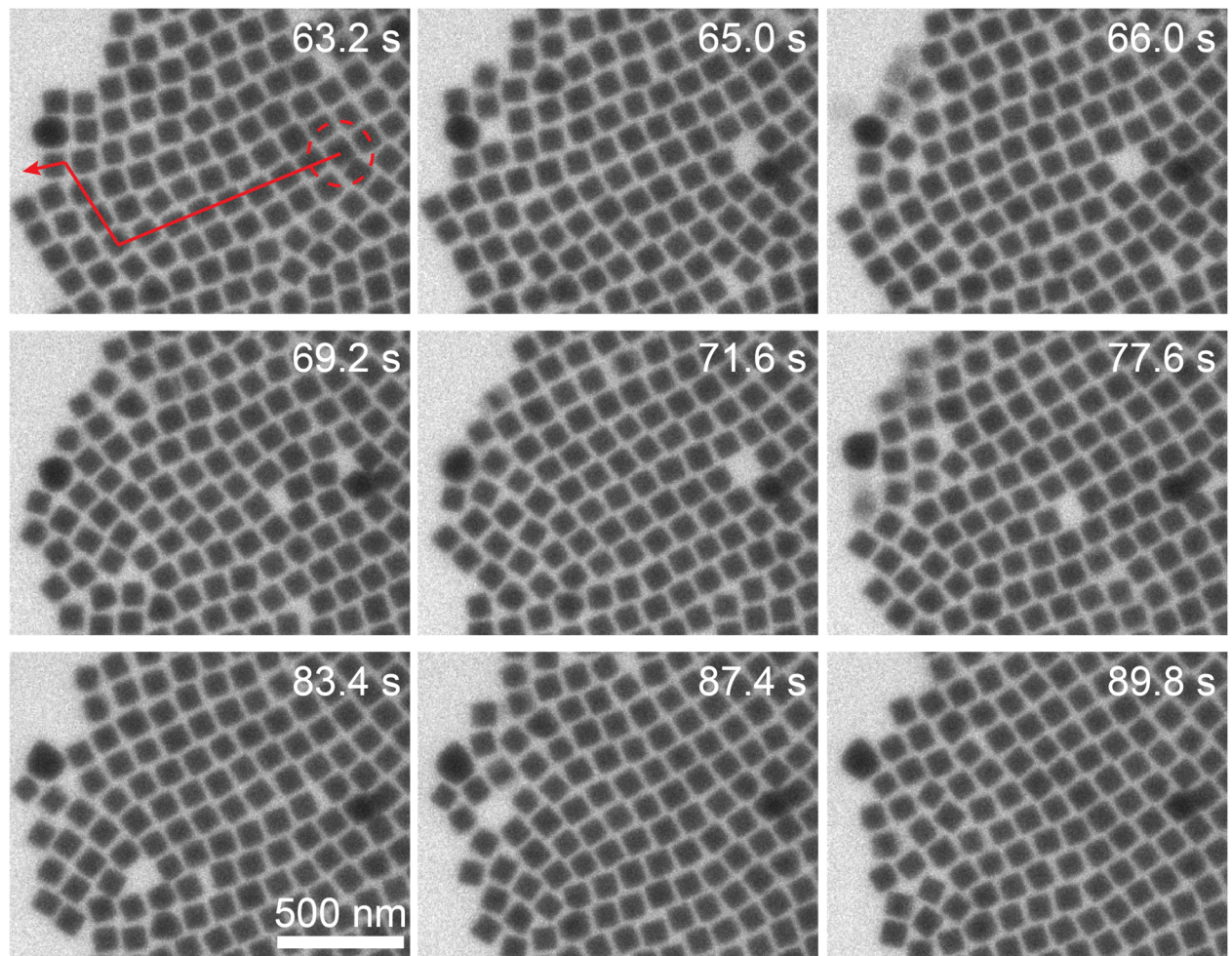
Supplementary Figure 10. **Quantitative analysis of translational and orientational order of the hexagonal rotator phase**. (a) Raw LCTEM images and (b) the same images overlaid with particle centroids colored according to $|\phi_{4j}|$. (c) 2D scatter plots of order parameters $|\psi_{6j}|$ and $|\phi_{4j}|$ for the four different stages shown in (a). The red dots denote the mean values of $|\psi_{6j}|$ and $|\phi_{4j}|$. (d-e) Plots of $g(r)$ (d) and lattice angle distribution $p(\alpha)$ (e) at selected time points. (f) Plots of ensemble-averaged $|\psi_{6j}|$ and $|\phi_{4j}|$ versus time.
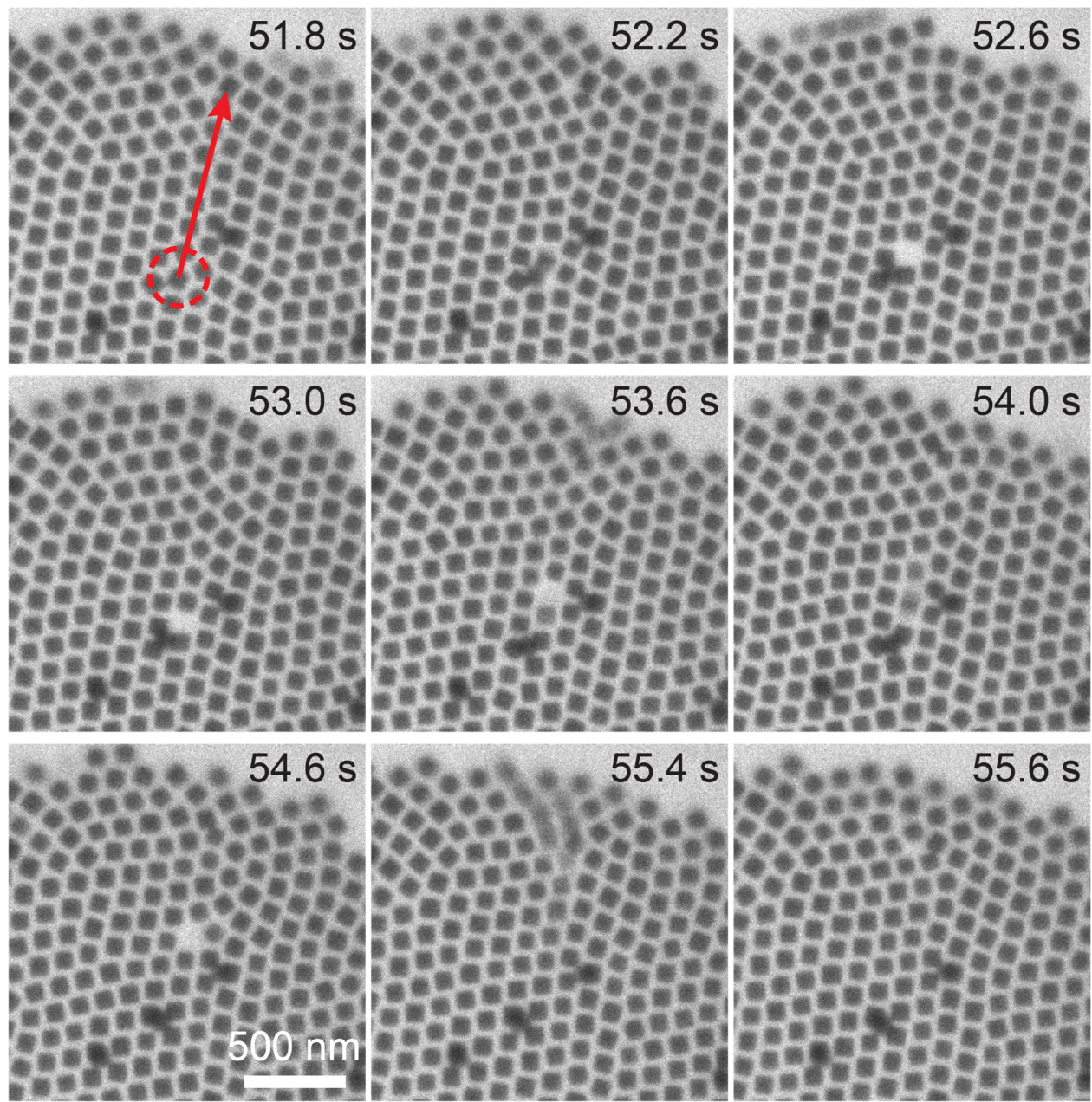
Supplementary Figure 11. **Quantitative analysis of translational and orientational order of the square-like phase**. (a) Raw LCTEM images and (b) the same images overlaid with particle centroids colored according to $|\phi_{4j}|$. (c) 2D scatter plots of order parameters $|\psi_{4j}|$ and $|\phi_{4j}|$ for the four different stages shown in (a). The red dots denote the mean values of $|\psi_{4j}|$ and $|\phi_{4j}|$. (d) Plots of $g(r)$ at selected time points. (e) Plots of ensemble-averaged $|\psi_{4j}|$ and $|\phi_{4j}|$ versus time.
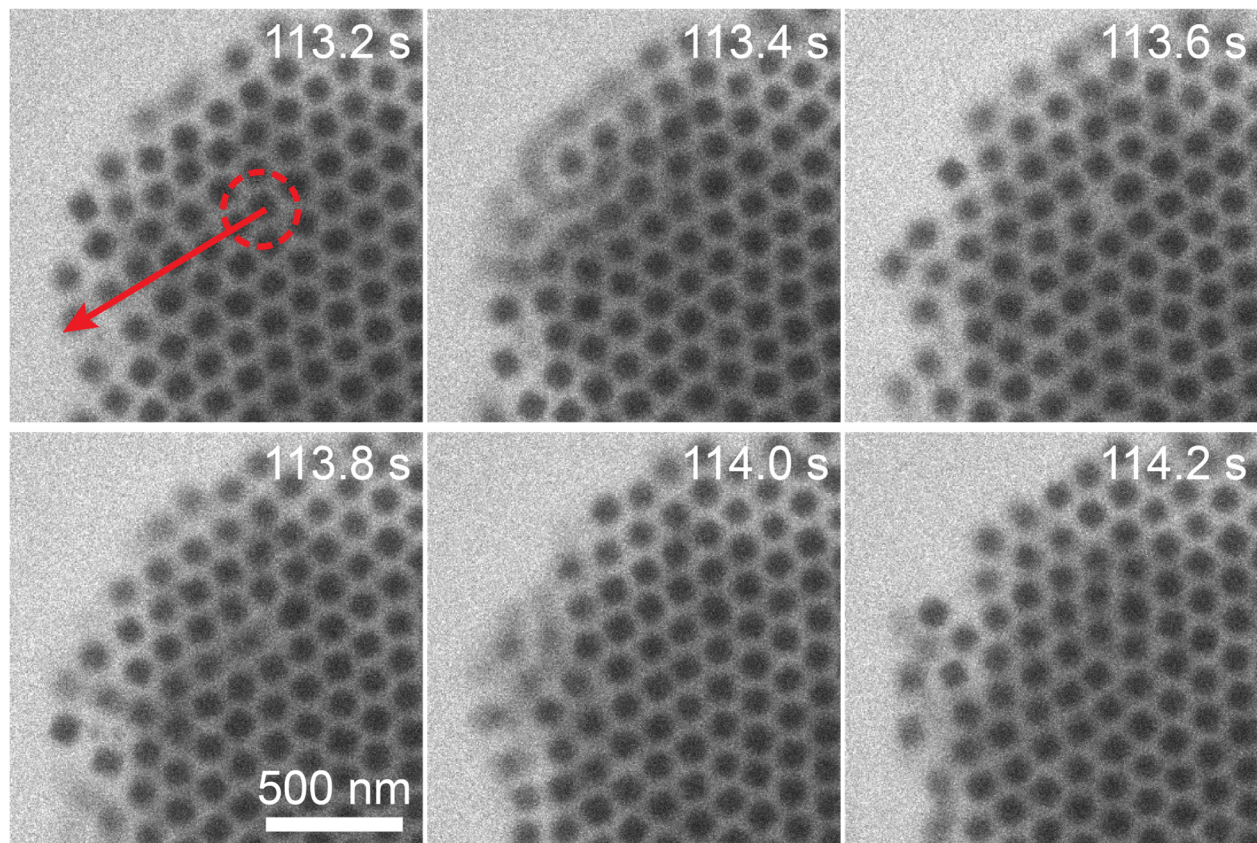
Supplementary Figure 12. Detachment of the square-like superlattice from the Si_3N_4 window after prolonged exposure to the electron beam. Time-lapse LCTEM images extracted from Supplementary Movie 8 showing that the superlattice membrane curled away from the Si_3N_4 window and departed the field of view. Electron dose rate: 14.0 $e^-\cdot\text{Å}^{-2}\cdot s^{-1}$.
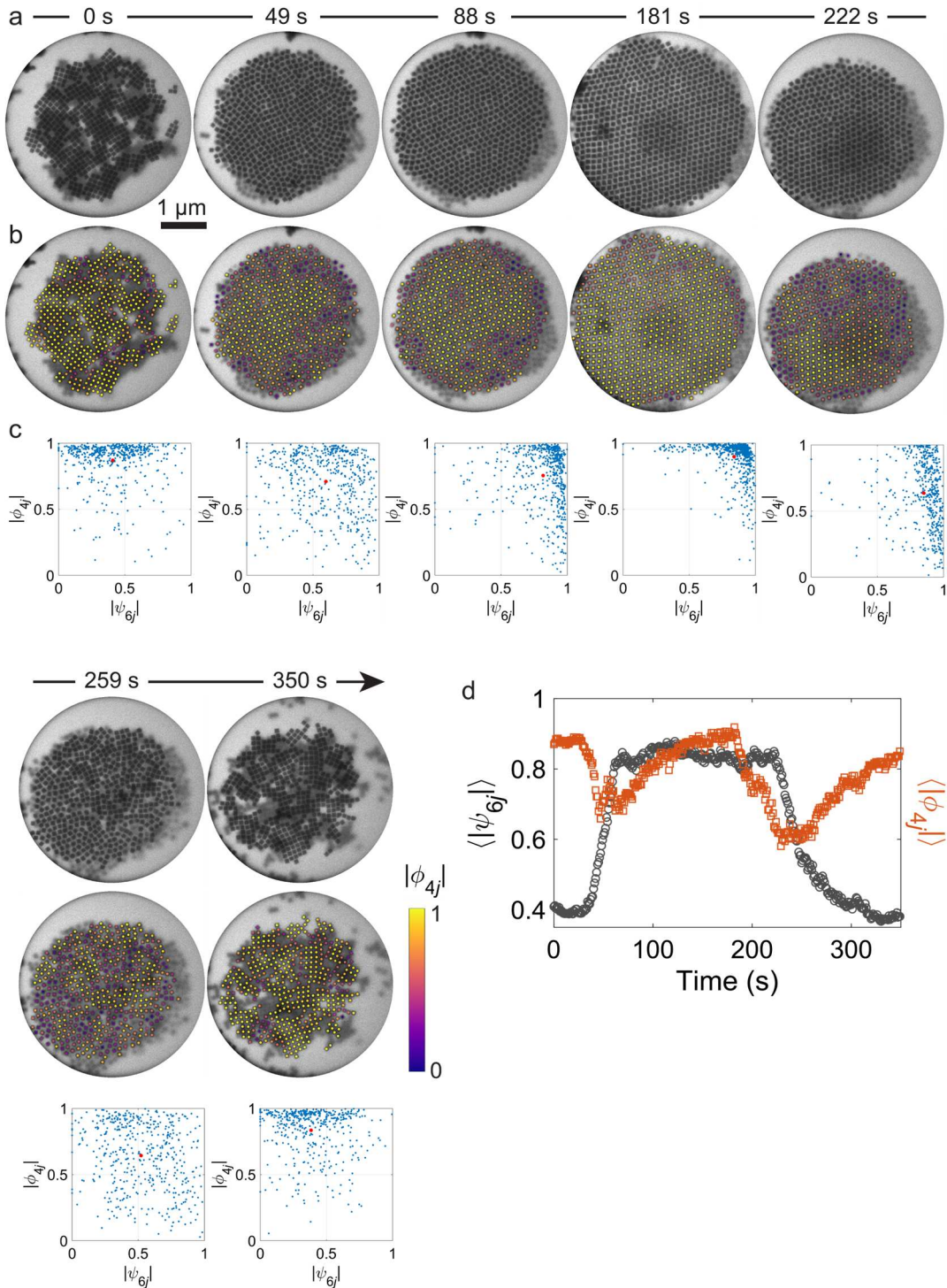
Supplementary Figure 13. **Vacancy formation and removal in the square-like superlattice**. Time-lapse LCTEM images extracted from Supplementary Movie 9. The dashed circle indicates the location of vacancy generation and the arrow depicts the pathway of vacancy migration.
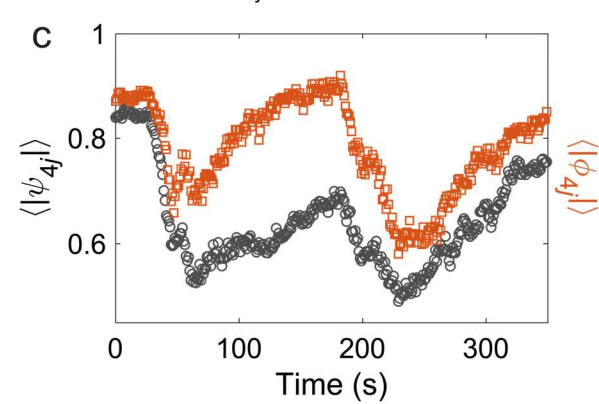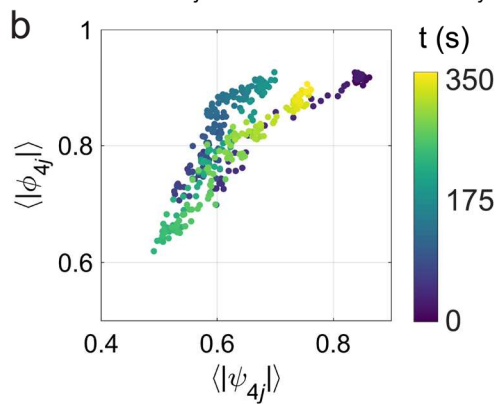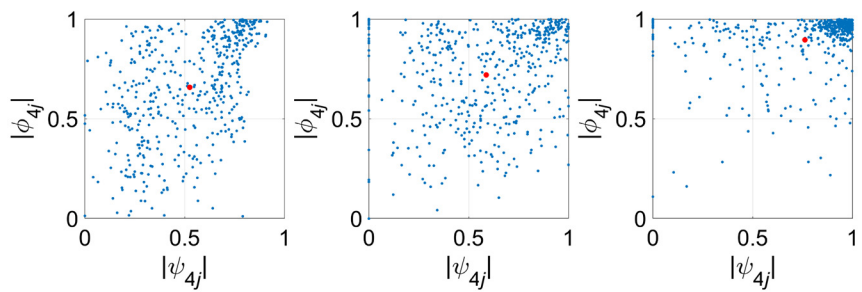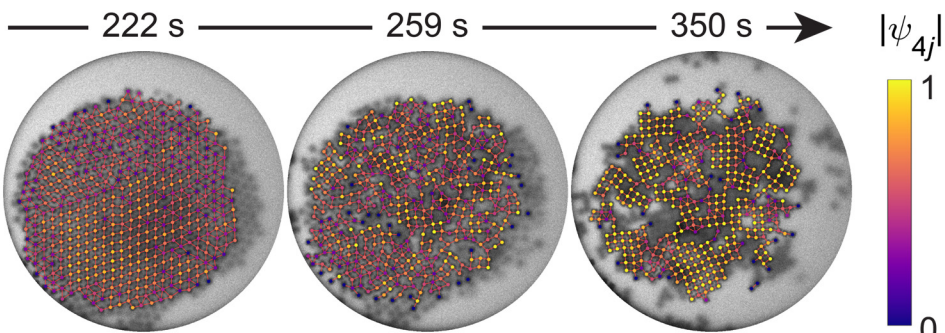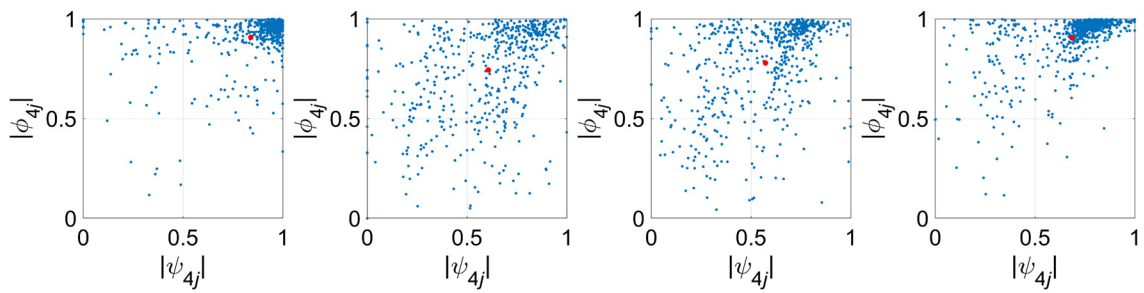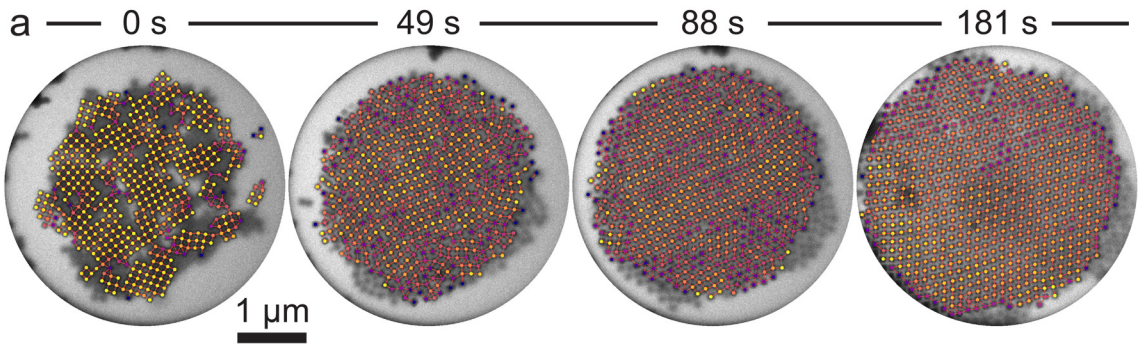
Supplementary Figure 14. Vacancy formation and removal in the rhombic superlattice. Time-lapse LCTEM images extracted from Supplementary Movie 9. The dashed circle indicates the location of vacancy generation and the arrow depicts the pathway of vacancy migration.
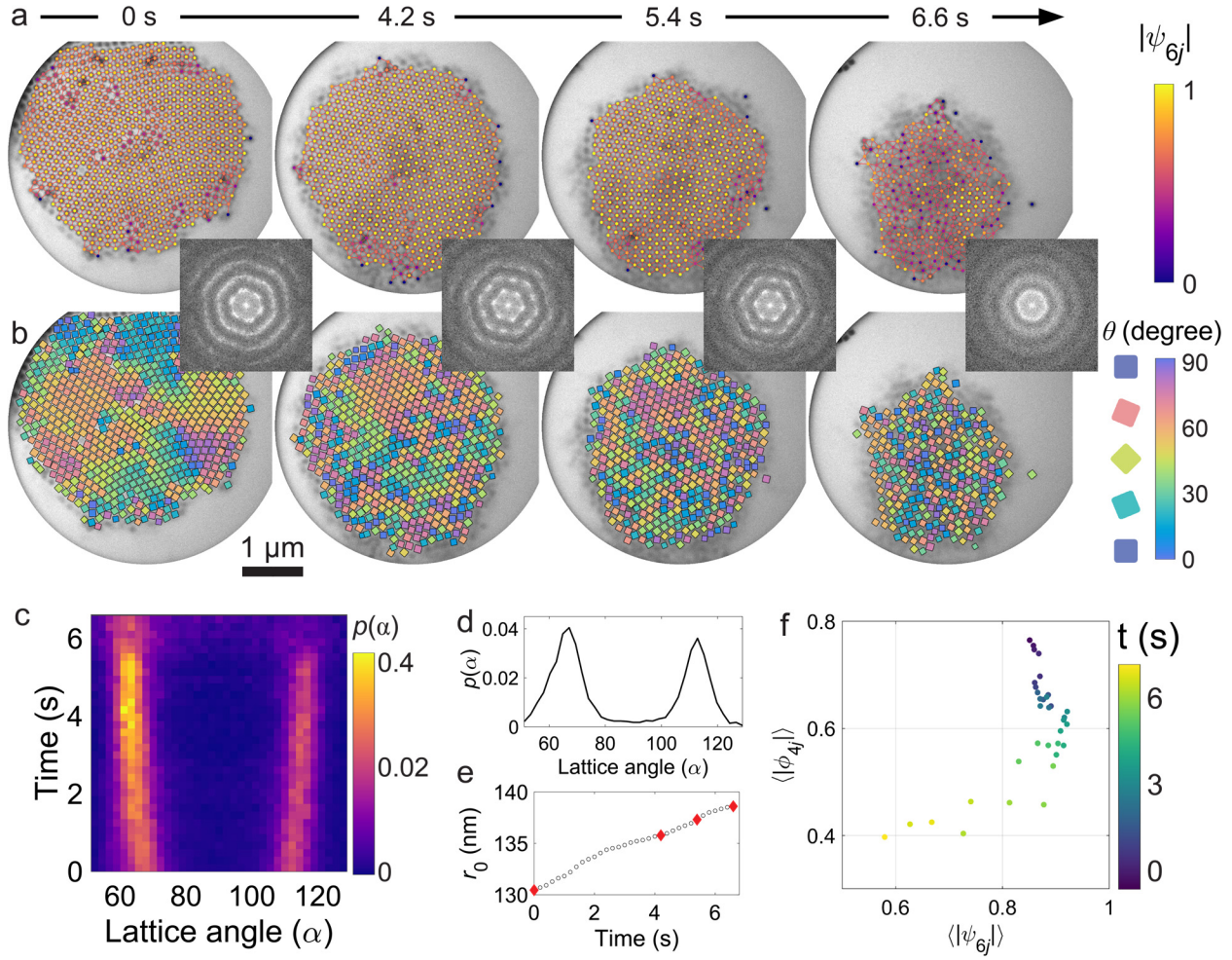
Supplementary Figure 15. **Vacancy formation and removal in the hexagonal rotator superlattice**. Time-lapse LCTEM images extracted from Supplementary Movie 9. The dashed circle indicates the location of vacancy generation and the arrow depicts the pathway of vacancy migration.
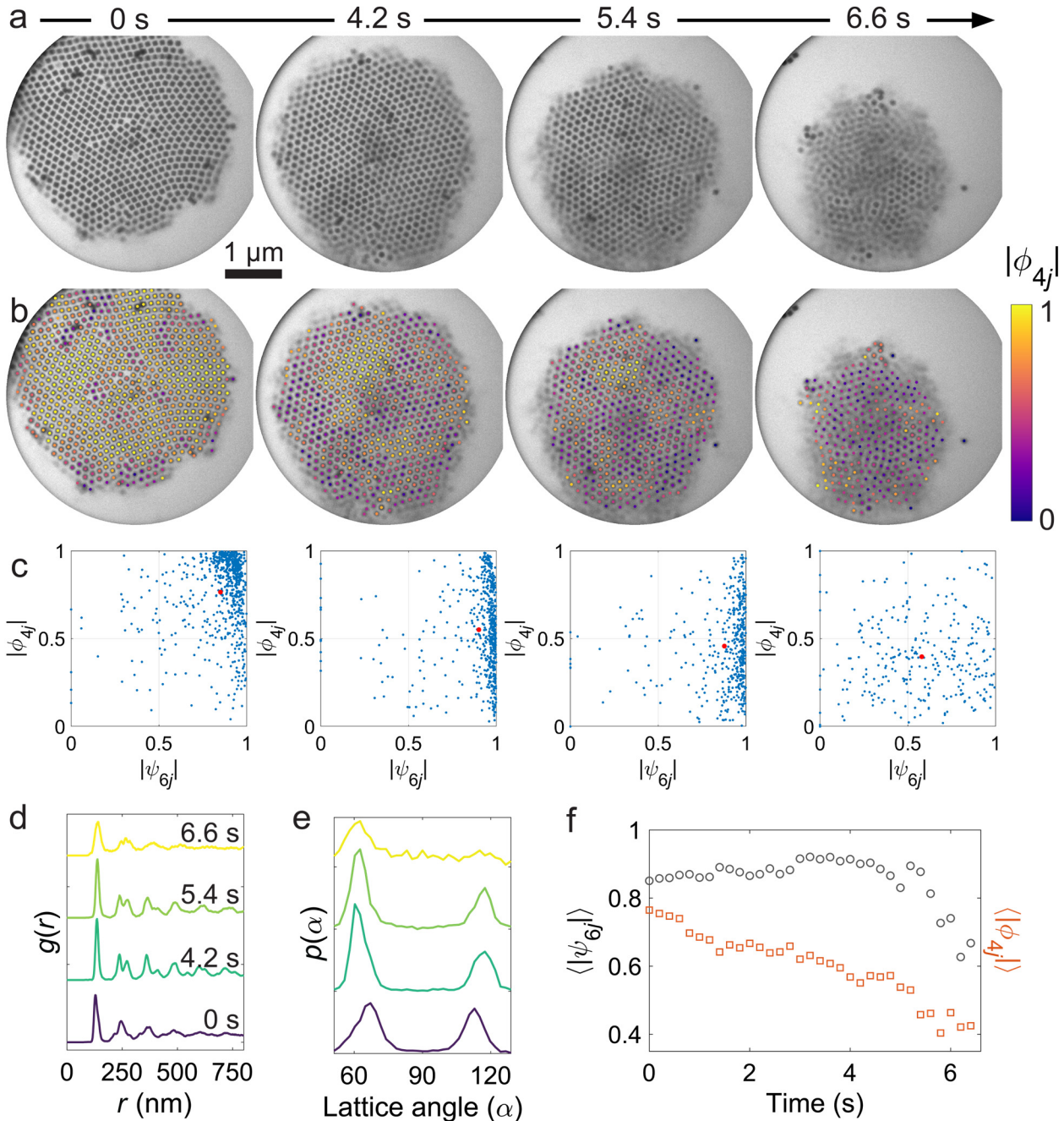
Supplementary Figure 16. Quantitative analysis of solvent-mediated reversible structural transitions between the square-like and the rhombic phases. (a) Raw LCTEM images and (b) the same images overlaid with particle centroids colored according to $|\phi_{4j}|$. (c) 2D scatter plots of $|\psi_{6j}|$ and $|\phi_{4j}|$ for the different stages shown in (a). The red dots denote the mean values of the order parameters. (d) Plots of ensemble-averaged $|\psi_{6j}|$ and $|\phi_{4j}|$ versus time.
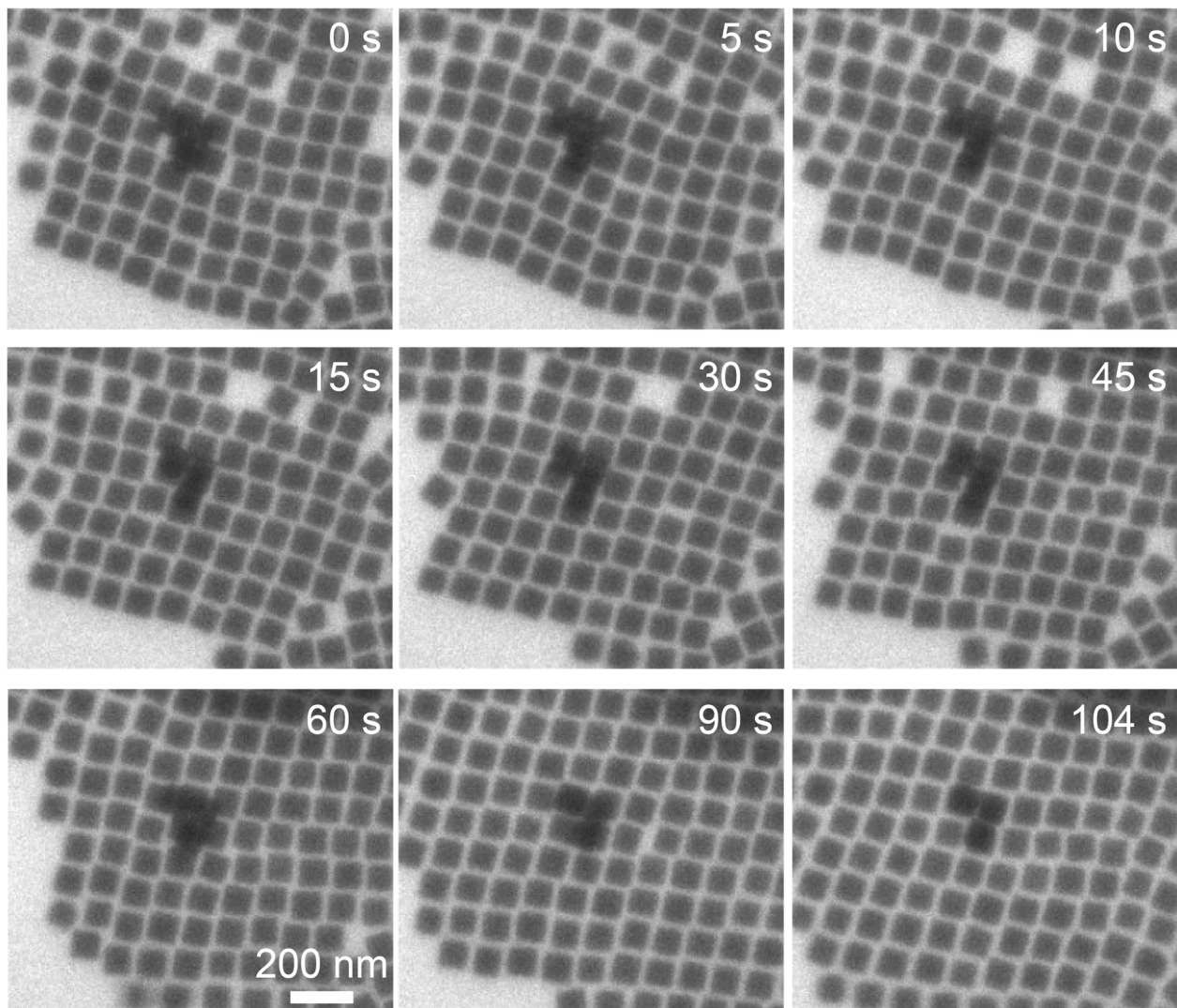
Supplementary Figure 17. Quantitative analysis of solvent-mediated reversible structural transitions between the square-like phase and the rhombic phase. (a) (top row) LCTEM images overlaid with particle centroids colored according to $\left|\phi_{4j}\right|$ and (bottom row) corresponding 2D scatter plots of $\left|\psi_{4j}\right|$ and $\left|\phi_{4j}\right|$ for the different stages of the transition. The red dots denote the mean values of the order parameters. (b) Trajectory plot of the ensemble-averaged order parameters $\left(\left\langle\left|\psi_{4j}\right|\right\rangle, \left\langle\left|\phi_{4j}\right|\right\rangle\right)$ versus time for the LCTEM movie. (c) Plots of ensemble-averaged $\left\langle\left|\phi_{4j}\right|\right\rangle$ and $\left\langle\left|\psi_{4j}\right|\right\rangle$ versus time.
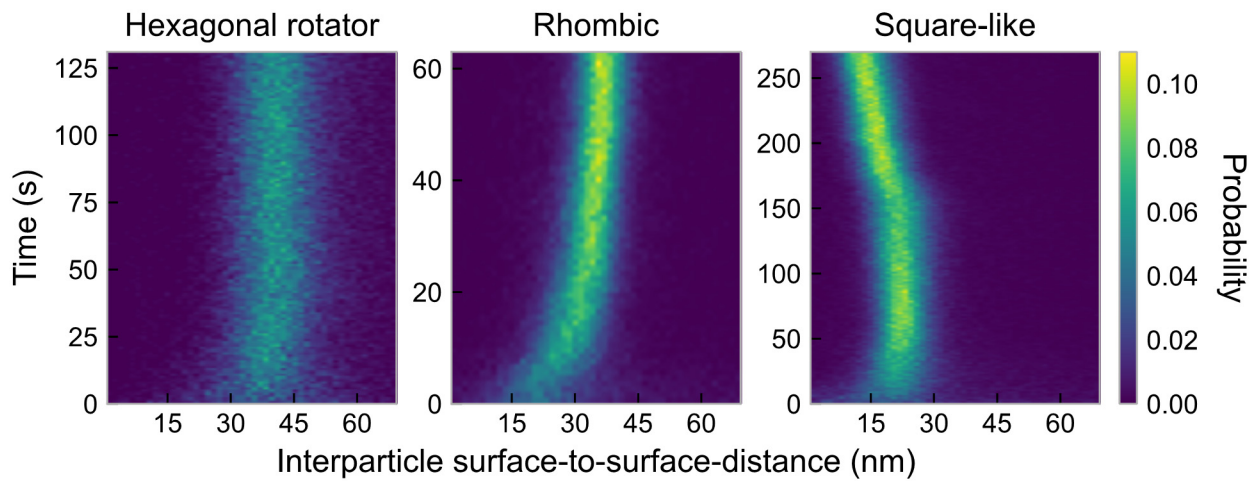
Supplementary Figure 18. Melting of the rhombic lattice induced by changing the solvent from medium-polarity (1:1 v/v octane/butanol) to low-polarity one (4:1 v/v octane/butanol). (a-b), Time-lapse LCTEM images and corresponding FFT patterns with (a) nanocube centroids colored according to $|\psi_{6j}|$ and (b) nanocubes colored according to their orientations. (c) Time-dependent lattice angle distribution. (d) Plot of lattice angle distribution of at t = 0 s. (e) Plot of nearest-neighbor distance retrieved from the first peak of $g(r)$ versus time. The red dots highlight the four stages shown in (a) and (b). (f) Trajectory plot of ensemble-averaged order parameters $|\psi_{6j}|$ and $|\phi_{4j}|$ versus time.
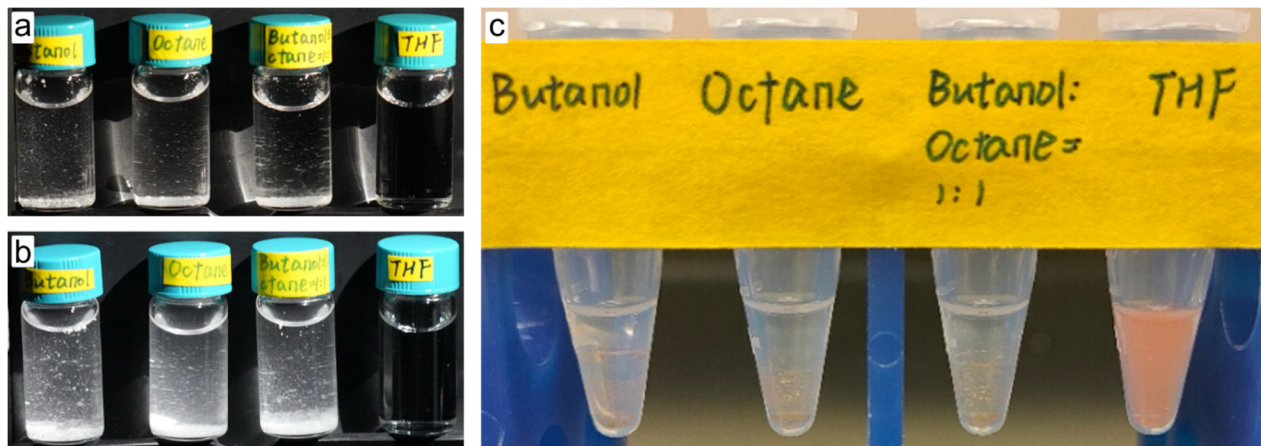
Supplementary Figure 19. Quantitative analysis of translational and orientational order during melting of the rhombic lattice induced by changing the solvent from medium-polarity (1:1 v/v octane/butanol) to low-polarity one (4:1 v/v octane/butanol). (a) Raw LCTEM images and (b) the same images overlaid with particle centroids colored according to $|\phi_{4j}|$. (c) 2D scatter plots of $|\psi_{6j}|$ and $|\phi_{4j}|$ for the four different stages shown in (a) and (b). The red dots denote the mean values of $|\psi_{6j}|$ and $|\phi_{4j}|$. (d-e) Plots of $g(r)$ (d) and lattice angle distribution $p(\alpha)$ (e) at selected time points. (f) Plots of ensemble-averaged $|\psi_{6j}|$ and $|\phi_{4j}|$ versus time.
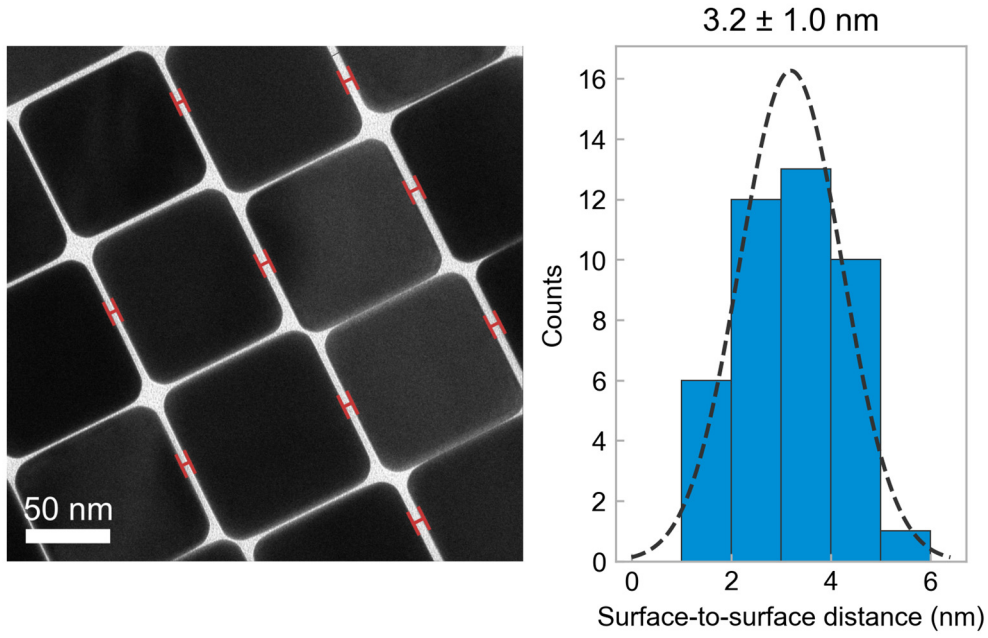
Supplementary Figure 20. Transition from the square-like to rhombic superlattice through continuous lattice distortion induced by solvent exchange. Time-lapse LCTEM images extracted from Supplementary Movie 14 showing that a small square-like domain gradually transformed into a rhombic lattice through collective rotation of nanocubes bypassing a hexagonal rotator-like intermediate. Note that the orientational order of nanocubes was largely maintained during the transition. Electron dose rate: 14.0 $e^-\cdot\text{Å}^{-2}\cdot s^{-1}$.

Supplementary Figure 21. Distributions of interparticle surface-to-surface distances during self-assembly into different phases. These interparticle distances were calculated by finding the shortest surface-to-surface distances between each nanocube and its four nearest neighbors. Nanocube positions and orientations were extracted from the LCTEM images of Supplementary Movies 4, 6, and 7 for the rhombic, hexagonal rotator, and square-like lattices, respectively.

Supplementary Figure 22. Evaluating the solubility of polystyrene in various solvents and its effects on the dispersibility of AuNCs. (a, b) Vials containing 1 mg/mL (a) and 4 mg/mL (b) of 3.2 kDa polystyrene in various solvents. (c) Samples of AuNCs in various solvents after sonication. From left to right in each image, the solvents are pure butanol, pure octane, 1:1 v/v butane/octane, and THF.

Supplementary Figure 23. Statistical analysis of interparticle surface-to-surface distance of polystyrene-grafted AuNCs dried onto a TEM grid. (left) Schematic of measurements of D_{dry}. Note that we measured D_{dry} along directions with the largest interparticle separations to obtain an upper bound for the mean D_{dry}. Several images were analyzed to calculate the mean D_{dry}. (right) Histogram of measured D_{dry}. The dashed line is a Gaussian fit to the histogram with a mean of 3.2 nm and a standard deviation of 1.0 nm.

Supplementary References

1   Zhong, Y., Allen, V. R., Chen, J., Wang, Y. & Ye, X. Multistep crystallization of dynamic nanoparticle superlattices in nonaqueous solutions. *J. Am. Chem. Soc.* **144**, 14915-14922 (2022).

2   Vold, M. J. Van der Waals' attraction between anisometric particles. *J. Colloid Sci.* **9**, 451-459 (1954).

3   De Rocco, A. G. & Hoover, W. G. On the interaction of colloidal particles. *Proc. Natl. Acad. Sci. U.S.A.* **46**, 1057-1065 (1960).

4   Anderson, J. A., Glaser, J. & Glotzer, S. C. Hoomd-blue: A python package for high-performance molecular dynamics and hard particle monte carlo simulations. *Comput. Mater. Sci.* **173**, 109363 (2020).

5   Glaser, J., Zha, X., Anderson, J. A., Glotzer, S. C. & Travesset, A. Pressure in rigid body molecular dynamics. *Comput. Mater. Sci.* **173**, 109430 (2020).

6   Adorf, C. S., Dodd, P. M., Ramasubramani, V. & Glotzer, S. C. Simple data and workflow management with the signac framework. *Comput. Mater. Sci.* **146**, 220-229 (2018).

7   Ramasubramani, V., Adorf, C., Dodd, P., Dice, B. & Glotzer, S. in *Proceedings of the Python in Science Conference.*

8   Ramasubramani, V. et al. Freud: A software suite for high throughput analysis of particle simulation data. *Comput. Phys. Commun.* **254**, 107275 (2020).

9   Bhattacharya, K. On the dependence of charge density on surface curvature of an isolated conductor. *Phys. Scr.* **91**, 035501 (2016).

10 O'Brien, M. N., Jones, M. R., Brown, K. A. & Mirkin, C. A. Universal noble metal nanoparticle seeds realized through iterative reductive growth and oxidative dissolution reactions. *J. Am. Chem. Soc.* **136**, 7603-7606 (2014).

11 Nikoobakht, B. & El-Sayed, M. A. Preparation and growth mechanism of gold nanorods (nrs) using seed-mediated growth method. *Chem. Mater.* **15**, 1957-1962 (2003).

12 Choueiri, R. M. et al. Surface patterning of nanoparticles with polymer patches. *Nature* **538**, 79-83 (2016).

13 Perez Cardenas, M. T. et al. Immobilized seed-mediated growth of two-dimensional array of metallic nanocrystals with asymmetric shapes. *ACS Nano* **12**, 1107-1119 (2018).

14 Dong, D., Fu, R., Shi, Q. & Cheng, W. Self-assembly and characterization of 2d plasmene nanosheets. *Nat. Protoc.* **14**, 2691-2706 (2019).

15 Israelachvili, J. N. *Intermolecular and surface forces* 162 (Academic Press, 2011).

16 Sánchez-Iglesias, A. et al. Hydrophobic interactions modulate self-assembly of nanoparticles. *ACS Nano* **6**, 11059-11065 (2012).

17 Santos, P. J., Gabrys, P. A., Zornberg, L. Z., Lee, M. S. & Macfarlane, R. J. Macroscopic materials assembled from nanoparticle superlattices. *Nature* **591**, 586-591 (2021).

18 Mark, J. E. *Physical properties of polymer handbook*. 2nd edn, (Springer New York, NY, 2007).

19 Ianiro, A. et al. Liquid–liquid phase separation during amphiphilic self-assembly. *Nat. Chem.* **11**, 320-328 (2019).

20 Israelachvili, J. N. *Intermolecular and surface forces* 390 (Academic Press, 2011).

21 Zheng, H. et al. Observation of single colloidal platinum nanocrystal growth trajectories. *Science* **324**, 1309-1312 (2009).

22 Lu, J., Aabdin, Z., Loh, N. D., Bhattacharya, D. & Mirsaidov, U. Nanoparticle dynamics in a nanodroplet. *Nano Lett.* **14**, 2111-2115 (2014).

23 Ye, X. et al. Single-particle mapping of nonequilibrium nanocrystal transformations. *Science* **354**, 874-877 (2016).

24 Loh, N. D. et al. Multistep nucleation of nanocrystals in aqueous solution. *Nat. Chem.* **9**, 77-82 (2017).

25 Chen, L. et al. Imaging the kinetics of anisotropic dissolution of bimetallic core-shell nanocubes using graphene liquid cells. *Nat. Commun.* **11**, 3041 (2020).

26 Hauwiller, M. R. et al. Tracking the effects of ligands on oxidative etching of gold nanorods in graphene liquid cell electron microscopy. *ACS Nano* **14**, 10239-10250 (2020).

27 Ronneberger, O., Fischer, P. & Brox, T. in *MICCAI International Conference.* 234-241 (Springer).

28 Buslaev, A. et al. Albumentations: Fast and flexible image augmentations. *Information* **11**, 125 (2020).

29 Gray, A. T., Mould, E., Royall, C. P. & Williams, I. Structural characterisation of polycrystalline colloidal monolayers in the presence of aspherical impurities. *J. Phys.: Condens. Matter* **27**, 194108 (2015).

30 Steinhardt, P. J., Nelson, D. R. & Ronchetti, M. Bond-orientational order in liquids and glasses. *Phys. Rev. B* **28**, 784-805 (1983).

31 Lavergne, F. A., Aarts, D. G. A. L. & Dullens, R. P. A. Anomalous grain growth in a polycrystalline monolayer of colloidal hard spheres. *Phys. Rev. X* **7**, 041064 (2017).

32 Ramananarivo, S., Ducrot, E. & Palacci, J. Activity-controlled annealing of colloidal monolayers. *Nat. Commun.* **10**, 3380 (2019).

33 Zhou, C., Shen, H., Tong, H., Xu, N. & Tan, P. Coupling between particle shape and long-range interaction in the high-density regime. *Chin. Phys. Lett.* **37**, 086301 (2020).

34 Lee, W. C., Kim, B. H., Choi, S., Takeuchi, S. & Park, J. Liquid cell electron microscopy of nanoparticle self-assembly driven by solvent drying. *J. Phys. Chem. Lett.* **8**, 647-654 (2017).

35 Mickel, W., Kapfer, S. C., Schröder-Turk, G. E. & Mecke, K. Shortcomings of the bond orientational order parameters for the analysis of disordered particulate matter. *J. Chem. Phys.* **138**, 044501 (2013).

36 Ou, Z., Wang, Z., Luo, B., Luijten, E. & Chen, Q. Kinetic pathways of crystallization at the nanoscale. *Nat. Mater.* **19**, 450-455 (2020).

37 Meijer, J.-M. et al. Convectively assembled monolayers of colloidal cubes: Evidence of optimal packings. *Langmuir* **35**, 4946-4955 (2019).

38 Zhao, K., Bruinsma, R. & Mason, T. G. Entropic crystal–crystal transitions of brownian squares. *Proc. Natl. Acad. Sci. U.S.A.* **108**, 2684 (2011).